Assimilation of Radar Radial Velocity with GSI-Based Hybrid 3DEnVar System for Improved Precipitation Forecasts

Donald E. Lippi

A scholarly paper in partial fulfillment of the requirements for the degree of

Master of Science

May 2016

Department of Atmospheric and Oceanic Science, University of Maryland
College Park, Maryland

Advisors: Dr. Daryl T. Kleist and Dr. Jacob R. Carley

Table of Contents

Abstract

The initialization of a dynamically consistent storm-scale environment with respect to both reality and the numerical model and of which results in a useful forecast presents a major challenge for convective-scale numerical weather prediction (NWP; Sun 2005; Stensrud et al. 2013; Johnson et al. 2015). Among the most critical sets of observations that can be used for initializing storm-scale NWP systems comes from the United States Weather Surveillance Radar-1988 Doppler (WSR-88D) network. This study will briefly evaluate the current capabilities of the using a GSI-based three-dimensional ensemble-variational (3DEnVar) radial wind procedure using a high-resolution, rapidly updating forecast system during a heavy precipitation event on 30-31 October 2015. A set of experiments was conducted to evaluate the sensitivity of the analysis to the super-observation settings, horizontal de-correlation length scale, and the velocity azimuthal display quality control to gain an understanding of how these parameters/quality control affect the resulting analysis from the radial wind assimilation. The results of this study will provide insight into future work for improving this procedure and more importantly improving the forecast of convective storms and precipitation.

Acknowledgements

I am grateful to everyone who has helped me reach this point in my career. Foremost, I would like to thank my academic advisor Dr. Daryl T. Kleist and my co-mentor from NOAA/Environmental Model Center (EMC) Dr. Jacob R. Carley. Without their continuous support and guidance, this work would not have been possible. I would also like to thank the EMC and I. M. Systems Group for supporting and funding this work. I am especially grateful to Geoff DiMego and Mike Pecnick for their understanding and support as I continue to pursue my education. I would also like to thank the rest of the EMC staff who have always been very kind and willing to provide assistance. Finally, I wish to acknowledge the love and encouragement of my family. I would like to extend my thanks to Jessica Meggitt who has been there since the beginning. Her love and patience have played a special role throughout my education.

List of Figures

List of Tables

Chapter 1. Introduction and Background

Convective-scale data assimilation (DA) continues to be an emerging field and has important societal implications as it has the potential to improve the prediction of hazardous weather. A few distinct differences exist between convective- and large-scale DA, the most prominent of which are faster error growth, lower predictability, and the lack of appropriate balance constraints (Droegmeier 1997; Sun 2005). The initialization of a dynamically consistent storm-scale environment with respect to both reality and the numerical model and of which results in a useful forecast presents a major challenge for convective-scale numerical weather prediction (NWP; Sun 2005; Stensrud et al. 2013; Johnson et al. 2015).

The prediction of a particular scale of atmospheric motion not only requires a model with sufficient resolution and an accurate representation of the major processes at those scales, but also requires that model to be initialized by assimilating observations that can describe that scale (Sun 2005). One such observational data set in particular for convective-scales, and is the focus of this study (although other observations are important), comes from the United States Weather Surveillance Radar 1988 Doppler (WSR-88D) network in the form of radial velocity (or radial wind).

Extensive work has already been done to assimilate radial wind observations. Some of this work has been focused on improving the resulting NWP forecasts of convective storms over a variety of DA systems. For example, Gao et al. (2004); Liu et al. (2005); Xiao et al. (2005); Hu et al. (2006); Stensrud and Gao (2010); and Ge et al. (2012) have all used a three-dimensional variational (3DVar) approach with some success. The 3DVar method, while it is more computationally attractive, has a major limitation that it only incorporates a static background error covariance. Encouraging results have also been seen using an ensemble Kalman filter (EnKF) method (Snyder and Zhang 2003; Dowell et al. 2004; Caya et al. 2005; Tong and Xue 2005; Gao and Xue 2008; Jung et al. 2008; Xue et al. 2008; Aksoy et al. 2009; Dowell and Wicker 2009; Lu and Xu 2009; Aksoy et al. 2010; Yussouf and Stensrud 2010). The advantage of the EnKF over 3DVar is that it dynamically evolves the background error statistics through the use of an ensemble forecast. The EnKF method also has limitations due to the ensemble size relative to the

degrees of freedom for the NWP model. To overcome these challenges, a hybrid method (Lorenc 2003) is suggested which uses a blend of the static and ensemble background error covariances. A few studies have shown that the use of a hybrid DA system may provide the best results for convective-scale forecasting (Carley 2012; Li et al. 2012; Gao and Stentrud 2014; Johnson et al. 2015). Other studies have focused on deriving appropriate observational errors to make better use of the observations (Rihan et al. 2008; Simonin et al. 2014; Waller et al. 2015a; 2015b).

Historically, assimilating radial wind observations in the 12-km North American Mesoscale (NAM) forecast system (Rogers et al. 2009; and its predecessor the Eta model) have generally shown to have a neutral impact on the resulting forecast (Carley, personal communication). Motivated by the successes of assimilating radial wind observations for convective-scale NWP in previous work and yet lack of benefit currently obtained in regional applications of the grid point statistical interpolation system (GSI; Wu et al. 2002; Kleist et al. 2009), active research will be done to extend the most current methods for radial wind assimilation to the GSI. This preliminary work will primarily focus on tuning the current implementation of radial wind assimilation in the GSI to evaluate if it can provide any benefit in a regional, rapidly updating, high-resolution model in a retrospective case study of a heavy precipitation event. Three areas of focus within the context of the GSI radial wind assimilation procedure will be examined: the velocity azimuth display (VAD) wind quality control (VADqc), the super-observation[1] density, and the horizontal de-correlation length scale used to approximate the off-diagonal terms in the static background error covariance matrix.

In a prior study, Liu et al. (2005) assimilated radial wind observations in an 8-km version of the WRF-NMM via GSI-based 3DVar. They super-obbed radial wind observations from five different radars to a regular grid at resolutions of 0.05, 0.1, 0.25, and 0.5 degrees (which corresponds to about 4.55, 9.1, 22.75, and 45.5-km respectively) to test the impacts of increasing the super-ob density on the analysis and on a short forecast. They showed that by increasing the density of the super-obs (i.e., smaller super-ob boxes), more detailed structure is retained thus resulting in an analysis closer to the

[1] The term for a surrogate datum that replaces several partially redundant actual data is a "super-observation" sometimes referred to as a "super-ob" (Purser et al. 2000).

observations. Their results only showed one 6-hour forecast, which may have been too long to see any real benefit using 3DVar where the advantage from radar DA is ~1-hr (Johnson et al. 2015). It was not demonstrated whether the benefit from the radial wind observations was retained in the resulting forecast during a shorter forecast period. Increasing the resolution also increased the computational cost of the analysis; therefore, finding a balance between the cost and the quality of the analysis is necessary. Their results also revealed that if the de-correlation length is too large for the analysis of radar data, the analysis will become unreasonably smooth thus losing the convective-scale structures that might be present in the data. Furthermore, this causes grid points far away from the observation to be incorrectly influenced. Another result of their work was the use of the VAD winds as a quality control marker, which may discard observations that might be worth keeping.

Since then, the National Center for Environmental Prediction (NCEP) has developed more sophisticated regional numerical forecast systems, which could greatly benefit from an improved radial wind assimilation procedure than what is currently available in the GSI. Furthermore, an extensive amount of work has been done in many other DA systems to assimilate radial wind observations whereas the GSI is much less mature in this regard. In this study, the current capabilities of the GSI radial wind procedure will be evaluated using a high-resolution, rapidly updating forecast system during a heavy precipitation event. The results of this study will provide insight into future work for improving this procedure and more importantly improving the forecast of convective storms and precipitation.

Chapter 2 will begin with a description of the numerical model, the data assimilation system and hybrid 3D ensemble-variational (hybrid 3DEnVar) cost function, the super-obbing procedure, and the experimental design. Chapter 3 presents the results of single-observation experiments testing the hybrid 3DEnVar configuration followed by the effects of super-obbing, and experiments assimilating super-observations from a single radar. These experiments test the effects of the VADqc, horizontal de-correlation length scale, and super-observation resolution. The next section contains results from the modifications in a retrospective forecast. Chapter 4 contains a summary and the conclusions of the experiments followed by Chapter 5 which discusses future work.

Chapter 2. Model Configurations and Experimental Design

2.1 Forecast Model

Retrospective weather forecasts were produced using the North American Mesoscale Rapid Refresh (NAMRR) forecast system (Carley et al. 2015). The NAMRR is an extension of the conventional NDAS/NAM forecast system (Rogers et al. 2014) and provides hourly analysis and forecast cycles over the NCEP operational NAM parent and CONUS nest computational domains (Fig. 2.1) using NCEP's non-hydrostatic multi-scale model on the B-grid (NMMB; Janjić and Gall 2012) dynamic core.

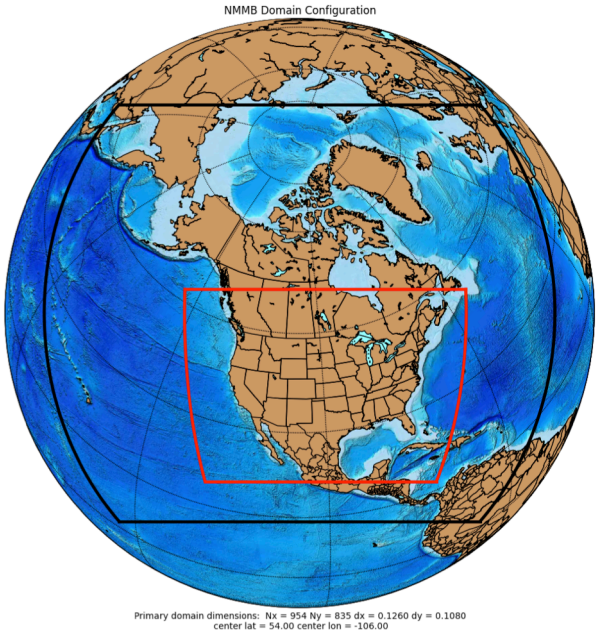

Fig. 2.1 Computational domains. The outer (black) and inner (red) domains are the 12-km parent and 3-km CONUS nest domains respectively.

For this study, the forecast model was configured to match a developmental version the NAMRR for consistency with the NCEP NAM v4 upgrade. The horizontal grid spacing of the outer parent domain was 12-km (954 × 835 grid points) and the inner nested CONUS domain was 3-km (1828 × 1466 grid points) (Fig. 2.1). Both domains were configured to use 60 atmospheric layers (61 model levels) using a hybrid sigma-pressure vertical coordinate system and a 2-hPa model top. The vertical coordinate changes from sigma to pressure at 300-hPa. The time steps were 25s for the 12-km parent domain and 6.25s for the 3-km CONUS nest. The following physical parameterizations were used: RRTM (Rapid Radiative Transfer Model; Iacono et al. 2008) for both long wave and short wave, Ferrier-Aligo (Aligo et al. 2014) for microphysics, Mellor-Yamada-Janjić (MYJ; Janjić 2001) for turbulence and the surface layer, Noah (Ek et al. 2003) for the land surface, and the Betts-Miller-Janjić (BMJ; Janjić 1994) for cumulus parameterization in the 12-km

parent, the 3-km nest is convection-allowing (no parameterized convection). Table 2.1 summarizes the parameterizations.

Table 2.1 Summary of the physical parameterizations used by the NMMB.

Domain	Grid space	Radiation (LW/SW)	Microphys.	Turbulence	Surface lyr.	Cumulus
Parent	12-km	RRTM	Ferrier-Aligo	MYJ	MYJ	BMJ
CONUSnest	3-km	RRMT	Ferrier-Aligo	MYJ	MYJ	None

2.2 Data Assimilation Cycling in the NAMRR

The data assimilation cycling procedure for the NAMRR is similar to that described in Djalalova et al. (2016) and graphically demonstrated by Fig. 2.2. DA is performed on both the 12-km parent and the 3-km CONUS nest domains (Fig. 2.1). The assimilation cycles are separated into two categories: catch-up and hourly. The catch-up cycles occur four times per day at the traditional cycle times (00, 06, 12, and 18 UTC). The catch-up cycles begin 6-hours prior to each cycle time (TM06; time minus 6 hours). At TM06, the NAMRR is partially cycled (Rogers et al. 2009) by using the first guess atmospheric state from the Global Data Assimilation System (GDAS) and the TM01 NAMRR forecasted land states from the previous catch-up cycle. Hourly analyses are then performed until TM00 when 60- and 84-hour forecasts are generated for the 3-km CONUS and 12-km North American domains, respectively. In the case of the experiments in this study, the catch-up cycle free forecast is reduced to a 36-hour forecast for both domains. Hourly cycles are then performed between each catch-up cycle and are fully cycled (i.e., uses both the atmospheric and land states from the previous cycle). For each hourly cycle, an 18-hour free forecast is generated for both domains.

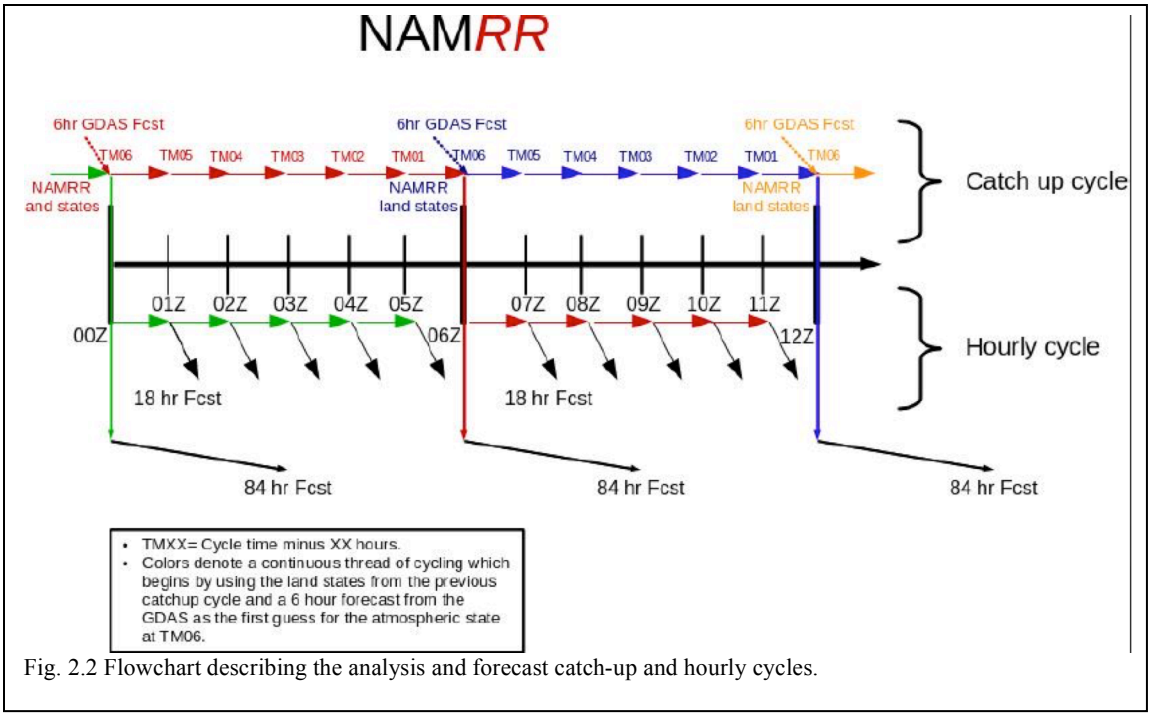

Fig. 2.2 Flowchart describing the analysis and forecast catch-up and hourly cycles.

2.3 The Grid Point Statistical Interpolation (GSI) Data Assimilation System

The gridpoint statistical interpolation (GSI; Wu et al. 2002; Kleist et al. 2009) system is a variational analysis system formulated in model grid space and is used in many operational applications at NCEP including the NAMRR forecast system. Additional information regarding the GSI can be found in the DTC GSI user manual online at http://www.dtcenter.org/com-GSI/users/docs/. For NAMRR applications, the GSI is configured using a hybrid 3-dimensional ensemble-variational (3DEnVar) algorithm (Wang et al. 2013; Kleist and Ide 2015a). Numerous studies (Wang et al. 2007, 2008; Liu et al. 2008, 2009; Zhang and Zhang 2012; Liu and Xiao 2013; Zhang et al. 2013; Kleist and Ide 2015a, 2015b) have suggested the use of a hybrid system (i.e., blended covariances) over the traditional variational or ensemble-based methods, which utilize exclusively a static or ensemble covariance respectively. The GSI hybrid is formulated using the variational framework and an ensemble covariance (EnVar; Lorenc 2013) blended with a static covariance.

2.4 Hybrid 3D Ensemble-Variational Cost Function

Variational methods determine the analysis (i.e., the most likely state given the prior forecast and observations) by the direct minimization of a cost function. Following the

notation of Ide et al. (1997) wherever possible, the hybrid 3DEnVar cost function may be written in incremental form as (see Wang 2010):

$$J(\boldsymbol{\delta x_f}, \boldsymbol{\alpha})=\beta_f \frac{1}{2}(\boldsymbol{\delta x_f})^T \mathbf{B_f}^{-1}(\boldsymbol{\delta x_f})+\beta_e \frac{1}{2}\sum_{n=1}^{N}(\boldsymbol{\alpha^n})^T \mathbf{L}^{-1}(\boldsymbol{\alpha^n})+\frac{1}{2}(H\boldsymbol{\delta x_t}-\mathbf{d})^T \mathbf{R}^{-1}(H\boldsymbol{\delta x_t}-\mathbf{d}). \quad (1)$$

The incremental form is used for simplicity and the analysis increments and the innovation are defined as follows

$$\boldsymbol{\delta x_f}=\mathbf{x_a}-\mathbf{x_b} \quad (2)$$

$$\boldsymbol{\delta x_t}=\boldsymbol{\delta x_f}+\sum_{n=1}^{N}[\boldsymbol{\alpha^n}\circ\boldsymbol{\delta x_e^n}] \quad (3)$$

$$\mathbf{d}=\mathbf{y^o}-\mathbf{H x_b} \quad (4)$$

The analysis increment derived from the static error covariance, $\boldsymbol{\delta x}_f$, measures the departure of the optimal state or analysis, $\mathbf{x_a}$, from the previous forecast or background, $\mathbf{x_b}$, and is weighted by the inverse of the static (fixed) background error covariance matrix, $\mathbf{B_f}$. The innovation or observation residual, $\mathbf{d}$, measures the departure of the observations, $\mathbf{y^o}$, and the background state by means of the non-linear, H and linear observation operators $\mathbf{H}$, and is weighted by the inverse of the observation error covariance, $\mathbf{R}$. The flow-dependent, ensemble estimated covariances are included in the cost function through the extended control variable method (Lorenc 2003; Buehner 2010). The extended control variable, $\boldsymbol{\alpha^n}$, is a scalar quantity used to scale the ensemble perturbation, $\mathbf{x_e^n}$ using a Schur product where N is the number of ensemble members and $\mathbf{L}$ denotes the error covariance for the alpha control variable and is specified to be of unit amplitude. The total analysis increment, $\boldsymbol{\delta x_t}$, is a linear combination of the analysis increment derived from the static error covariance and that which is derived from the ensemble perturbation prescribed by the alpha control variable. The tuning parameters, β_f^{-1} and β_e^{-1}, are used to control the weight given to the static or ensemble contributions respectively (e.g., $\beta_f^{-1}=0.25$ gives 25% of the weight to the static and 75% to the ensemble error covariance). These tuning parameters are currently assumed to sum to one in the GSI.

2.5 Background Error Statistics

Hybrid DA systems, use a blend of covariances: one part from static, climatological statistics and another from flow-dependent, ensemble estimated statistics. The static background error statistics were estimated using the National Meteorological Center's (NMC) method (Parrish and Derber 1992), which averages the differences between lagged forecast pairs (e.g., 24- and 48-hour forecasts) valid at the same time. The static background error covariance is formulated to vary vertically and latitudinally. The ensemble background error covariance is estimated by an ensemble of 80 members from the Global Data Assimilation System's (GDAS) ensemble Kalman filter (EnKF), which runs at T574 (~45-km at the equator). Estimating the background error covaraiances in this way introduces flow-dependence and provides multivariate correlations. These cross correlations between variables allow for increments of unobserved variables to be made by the observed variables. For example, a pressure observation may be able to update the precipitable water field if such correlation in the ensemble perturbation exists, where in just pure 3DVar, the increment would be zero without the introduction of balance relationships in $\mathbf{B_f}$, complex forward operators, and/or through constraint terms in the cost function. The flow-dependence allows for analysis increments to be spread in a more realistic direction (e.g., along a front vs. isotropically). For the pre-operational configuration of the NAMRR, the weighting between the static β_f^{-1} and the flow-dependent β_e^{-1} background error covariance are set to be 25% and 75% respectively. Wang et al. (2007) showed that the optimal weighting is dependent on the quality of the static or ensemble estimated BEC. It is generally more desirable to place a higher weight on the ensemble covariance (Zhang et al. 2013; Wang et al. 2013; Schwartz et al. 2014).

2.6 Doppler Radar Radial Winds and Super-Observations

In the U.S., there are 150 WSR-88D's and each can provide a single volume scan in about 5-min. Each volume scan includes elevation angles ranging from 0.5 to 14-degrees, with azimuthal and along beam range sampling resolution of 1-deg and 250-m respectively. Given the high spatial and temporal observation frequency, the number of radial wind observations may be on the order of 7×10^8 per day (Liu, personal communication), and are able to observe much finer scales of motion (~500-m) than can

be accurately resolved within most NWP models. The errors that arise from the disparity between observation and model resolution are known as errors of representativity.

Super-obbing is a common method to reduce the representativeness errors in observations. The current super-obbing method used in the GSI uses a simple spatial and temporal averaging of the observed values (Alpert and Kumar 2007), however, other methods exist (e.g., Lorenc 1981, which averages innovations). The averaging is performed over a super-ob box whose dimensions can be controlled via adjustable parameters including: the azimuth angle range, elevation angle range, radial range, time-window, max elevation angle, and the minimum number of samples. The featured super-ob parameters in the GSI are summarized in a later section by Table 3.1 with their associated default values.

In addition to representativeness errors, there are three other main sources errors associated with observations: instrument errors, observation operator errors, and data pre-processing errors. The observation errors are to some extent correlated, which may be dependent of the state and model resolution (Janjić and Cohn 2006; Waller 2013; Waller et al. 2014a,b). However, in many DA systems including the GSI, it is assumed that the radial wind observations errors are uncorrelated (i.e., the observation error covariance matrix is diagonal); however, this is not a fundamentally necessary assumption and may not make the best use of the observational data. To reduce the large number of observations and to satisfy the assumption of uncorrelated observation errors, the observations are super-obbed.

2.7 Experimental Design

A set of experiments was conducted to evaluate the sensitivity of the analysis to the super-observation settings, horizontal de-correlation length scale, and the VADqc to gain an understanding of how these parameters/QC affect the resulting analysis from the radial wind assimilation. The super-ob settings were first reduced in an experiment comparing the resulting super-obs with the Level-II radial wind observations to better understand the effects of each tuning parameter. Single observation experiments were then conducted by creating a single synthetic observation designed to have come from the Fort Hood, Texas radar (KGRK) to test the impact of the background error covariance structure from the assimilation system. Experiments using real observations only from KGRK were then

made to test the super-observation settings, de-correlation length scale, and the VADqc. These experiments use a 3-km NAMRR 1-hour forecast valid at 1800 UTC 30 October 2015 as the background forecast, an 80 member plus the mean 6-hr forecast from the 1200 UTC GDAS T574 EnKF valid at 1800 UTC, and assimilated only radial wind observation(s) from KGRK using the GSI-based 3DEnVar system.

Retrospective simulations using the settings tested by the previous experiments were then conducted using the NAMRR forecast system. The base line experiment mimics the pre-operational configuration of the NAMRR over a 48-hour period (0000 UTC 30 October 2015 – 0000 UTC 01 November 2015) and includes the integration over the full 12-km parent and 3-km CONUS nest domains. Data assimilation was performed on both the 12-km parent and the 3-km CONUS nest domains; however, the experimental modifications to the radial wind assimilation were only made on the CONUS nest domain.

Chapter 3. Results and Discussion

3.1 Single-Observation Test

A set of single-observation experiments were made to evaluate the background error covariance structure used in the assimilation system by creating a single synthetic observation designed to have come from the Fort Hood, Texas radar (KGRK) depicted by Fig. 3.1 with a value of 30.0 m s^{-1} (6.23 m s^{-1} above the background) and an observation error of 1.0 m s^{-1}.

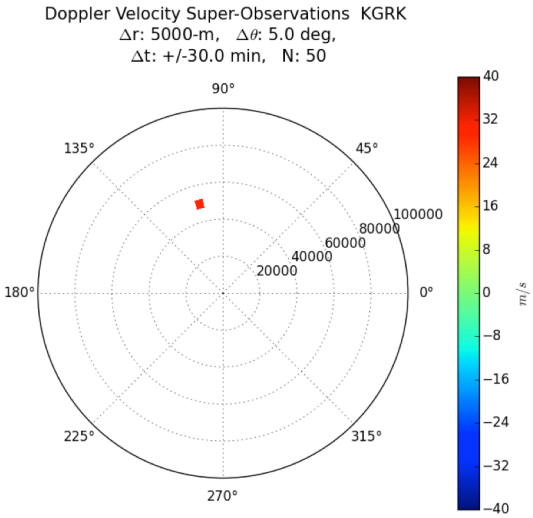

Fig. 3.1 Depiction of the single-observation value and position relative to the Fort Hood, Texas radar (KGRK; center). Distances from the center along the radial are given in meters. For reference, the location of KGRK is shown by Fig. 3.2 as the red star.

The first set of experiments test the weights for the static and ensemble error covariances to ensure that the hybrid configuration is working properly. The weighting factors β_f^{-1} and β_e^{-1} are designed to sum to one in the current formulation of the GSI hybrid. Under this assumption, setting the weight of the static error covariance to 1 (i.e., β_f^{-1}=1; β_e^{-1}=0) results in the system defaulting to 3DVar, which has no contribution from the ensemble error covariance. With this configuration, the increment should have a structure one would expect with 3DVar (i.e., quasi-isotropic; Fig. 3.2a). The background error covariance is usually prescribed to have such or similar characteristics because it has no knowledge of the uncertainty in the current background flow. Adjusting the weighting to the hybrid, pre-operational configuration where the contribution of the static background is 0.25 (i.e., β_f^{-1}=0.25; β_e^{-1}=0.75) shows a considerable impact to the analysis increment (Fig. 3.2b) with differences on the order of about +/-2.0 m s^{-1} (Fig. 3.2c). Giving weight to the ensemble covariance introduces flow-dependent characteristics into the analysis increment. Additional adjustment of the weightings to the other end of the spectrum giving 0 weight to the static covariance (i.e., β_f^{-1}=0; β_e^{-1}=1) results in the system defaulting to non-hybrid 3DEnVar which exclusively uses the ensemble covariance but still uses the

variational framework to compute the analysis increments. The difference between non-hybrid and hybrid 3DEnVar experiments (Fig. 3.2e) was much less than the difference between the 3DVAR solution and either 3DEnVar experiments (Fig. 3.2c). Thus, for the remainder of the sensitivity experiment, the pre-operational configuration with the static background weighted 25% will be used.

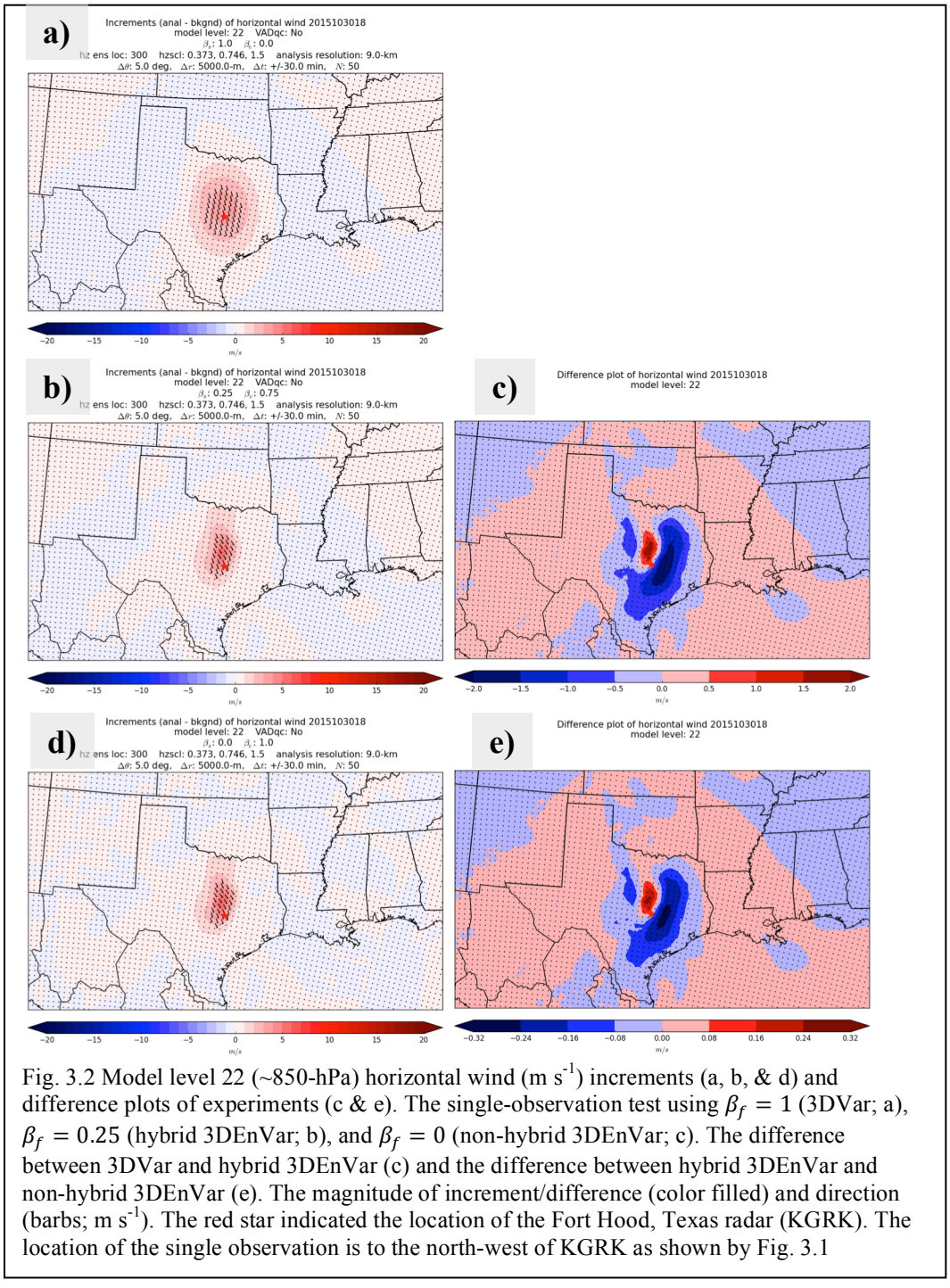

Fig. 3.2 Model level 22 (~850-hPa) horizontal wind (m s^{-1}) increments (a, b, & d) and difference plots of experiments (c & e). The single-observation test using $\beta_f = 1$ (3DVar; a), $\beta_f = 0.25$ (hybrid 3DEnVar; b), and $\beta_f = 0$ (non-hybrid 3DEnVar; c). The difference between 3DVar and hybrid 3DEnVar (c) and the difference between hybrid 3DEnVar and non-hybrid 3DEnVar (e). The magnitude of increment/difference (color filled) and direction (barbs; m s^{-1}). The red star indicated the location of the Fort Hood, Texas radar (KGRK). The location of the single observation is to the north-west of KGRK as shown by Fig. 3.1

3.2 Case Study Overview

Retrospective forecasts during the convectively active period 30-31 October 2015 in the southern plains were made to evaluate the impacts of the modifications to the radial wind assimilation. Future experiments will incorporate additional cases to more robustly evaluate the impacts of these modifications. This case was chosen because it consists of a fairly diverse set of forcing mechanisms including an upper-level short-wave trough, cold front, and interaction between the low-level jet (LLJ) and a warm front, and a pre-frontal confluence zone. Additionally, this case exhibited heavy precipitation, flooding, damaging winds, and several tornadoes. More than one foot of rain fell in less than 24-hours between Austin and San Antonio, Texas (Fig. 3.3), which caused extensive flooding throughout that region. Another line of heavy precipitation occurred later in the period near Houston, Texas and to the northeast. Several tornadoes rated between EF-0 and EF-2 were reported in these two regions on 30 October 2015. Heavy precipitation and tornadoes rated EF-0 to EF-1 were also reported on the 31st in Louisiana and Mississippi (Fig. 3.4).

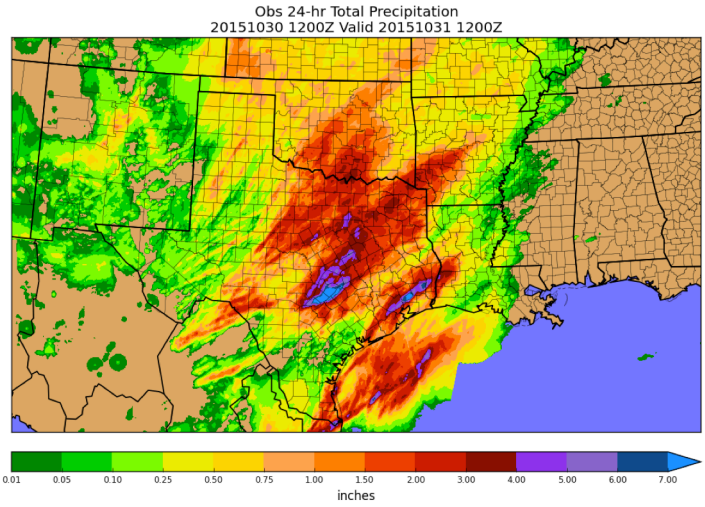

Fig. 3.3 Observed total 24-hour precipitation (inches) valid 20151031 1200Z (Hou et al. 2014)

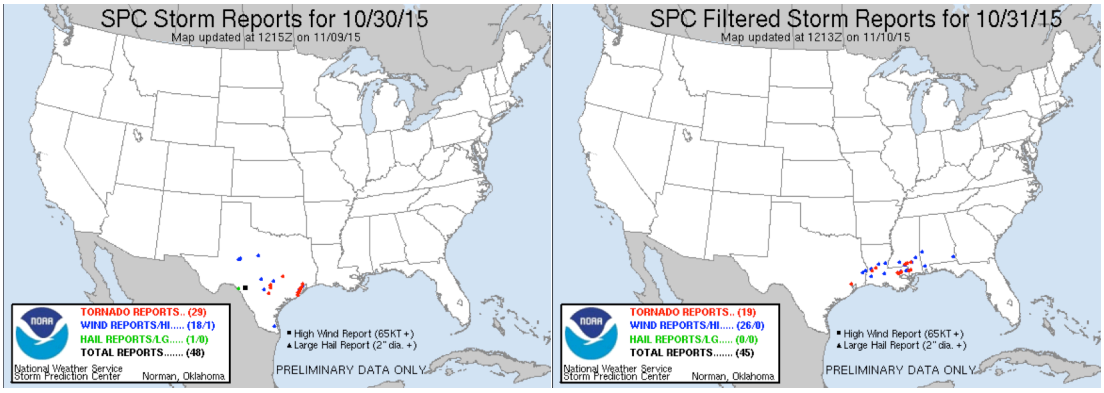

Fig. 3.4 Storm reports for 30-31 October 2015 from the Storm Prediction Center.

A deep, positively tilted upper-level trough was centered over the four corners region of Colorado, Utah, Arizona, and New Mexico and extended farther south into Mexico at 1200 UTC on 30 October 2015 (Fig. 3.5a, b). Associated with the upper-level trough was a well-defined 300 hPa jet streak (Fig. 3.5a) with winds in excess of 100 kts. An area of surface low pressure developed in response to the divergence associated with the upper-level forcing and was centered over New Mexico with a central low pressure of about 1002 hPa (Fig. 3.5d).

A warm/stationary front extended from the low pressure southeastward through central Texas (Fig. 3.5d). The presence of a 50 kt LLJ aided in destabilization of the warm sector enviornment by providing a rich transport of heat and moisture from the Gulf of Mexico into the low-levels of the region (Fig. 3.5c). The warm surface temperatures (high 70s) and dew-points (low 70s) helped to support an unstable environment having 1000+ J kg^{-1} mixed layer CAPE with values rising throughout the day. The region of intersection between the warm front and the LLJ resulted in a region favorable for super-cell development. A north-northeastward moving storm system approached this region and over the course of a few hours (1000 UTC to 1200 UTC on the 30th) intensified into a slow moving organized system. This lead to the majority of the precipitation over the Austin and San Antonio, Texas region as reflectivity values of 50 dBZ trained over this discrete area for several hours (1300 UTC to 1530 UTC).

To the west of this region, storms associated with the passage of the cold front began to initiate around 1500 UTC on the 30th . A pre- cold frontal boundary existed in the region of the warm moist air transport. As this boundary progressed southeastward throughout the day, it provided forcing for storms extending farther south near Corpus Cristi, Texas. A cluster of storms initiated from this boundary around 0300 UTC on the 31st just off the coast of Corpus Cristi in a region of confluent flow between this boundary and the on-shore winds and mixed layer CAPE around 1000-2000 J kg^{-1}. The motion of these storms was north-northeastward where they eventually moved onshore and interacted with the warm frontal boundary located near Houston, Texas. The strong 0-6 km shear associated with these storms supported the formation of mesocyclones especially after interacting with the warm front. This slow moving storm system trained for several hours (ahead of the cold front), which led to the majority of the heavy

precipiation in the Houston, Texas area. The cold front and the associated storms eventually caught up to the pre-frontal storms and formed a single line of strong convection which added to the total rainfall amounts for each of these areas.

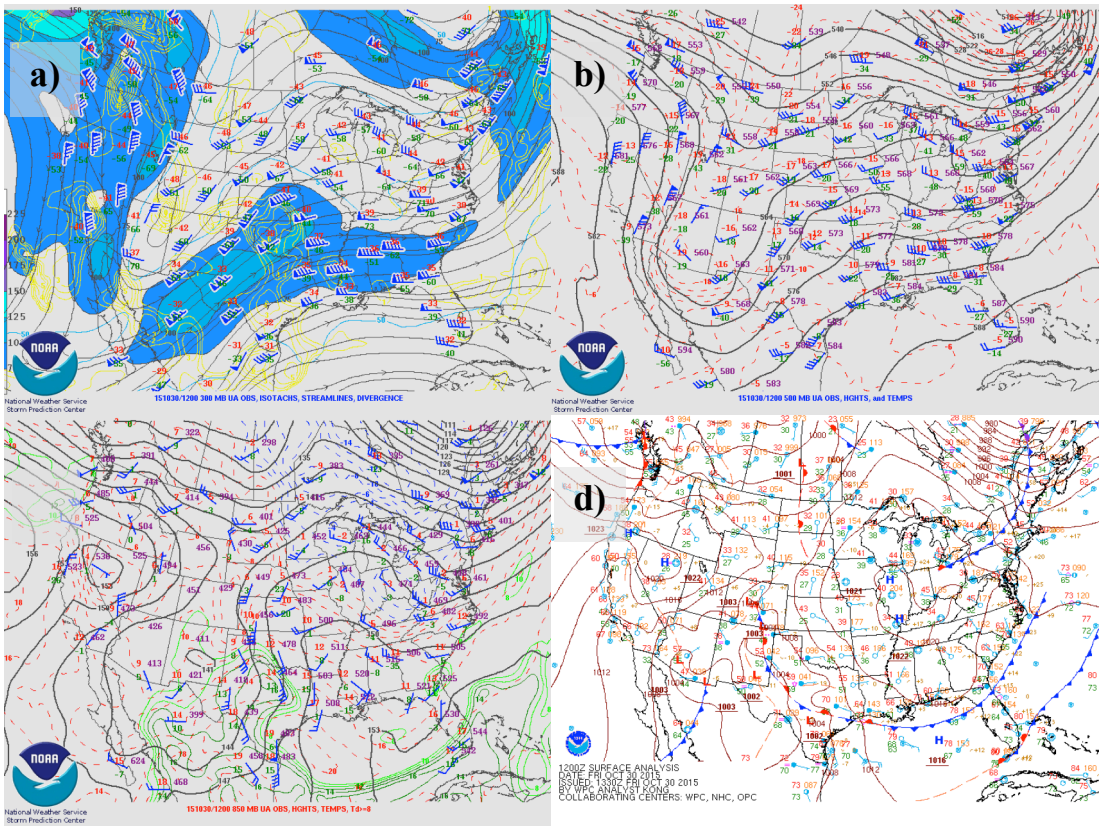

Fig. 3.5 Synoptic patterns at 1200 UTC 30 October 2015. Shown are maps of 300-hPa (a), 500-hPa (b), 850-hPa (c), and surface maps (d) from SPC. The 300-hPa maps color fill isotachs above 75-kts at 25-kts intervals, contoured stream lines (black), contour divergence (yellow), and wind barbs (kts). The 500-hPa maps contour geopotential height (black), temperature (dashed red), and wind barbs (kts). The 850-hPa maps contour geopotential heights (black), temperature (red/blue dashed for above/below freezing), dew points above 0 C, and wind barbs (kts). The surface maps contour isobars (brown) overlaid with high and low pressure centers, analyzed surface fronts, and surface observations.

3.3 Super-Obbing Observations from a Single Radar

The GSI internally processes the radial wind observations by means of a super-obbing technique (Alpert and Kumar 2007) to remove representativeness error and to help satisfy the assumption of uncorrelated observation errors (although it may not completely de-correlate them). The super-obbing procedure can be envisioned as a spatial and temporal averaging of the observations within a volume defined in radar coordinates by the tuning parameters in Table 3.1. The observation error ("thiserr") associated with the new super-observation is estimated using the square root of the variance of the observations within the super-ob box according to Eq. 5 (http://www.dtcenter.org/com-GSI/users/docs/).

$$thiserr = \sqrt{\left|\overline{V_r^2} - \overline{V_r}^2\right|} \tag{5}$$

Table 3.1 List of the super-observation parameters and their default and experimental values.

	Azimuth range (degrees)	Elevation angle range (degrees)	Radial range (meters)	One-half time range (hours)	Max elevation angle (degrees)	Minimum number of samples
	$\Delta\boldsymbol{\theta}$	$\Delta\boldsymbol{\varepsilon}$	$\Delta\boldsymbol{r}$	$\Delta\boldsymbol{t}$	$\boldsymbol{\varepsilon_{max}}$	$\boldsymbol{N}$
Default	5	0.25	5000	+/- 0.500	5	50
Experimental	2	0.25	2500	+/- 0.125	5	10

The effects of the super-ob parameters can be captured by visualizing the radar observations before (Fig. 3.6a) and after (Fig. 3.6b, c) the GSI has processed them as super-obs. Therefore, sensitivity experiments testing the effects of the super-ob parameters were made using observations from a single radar (KGRK) valid at 1800 UTC 30 October 2015. The experimental values for the super-observations were chosen because they were the smallest values that could be used at the time without using an unreasonable amount of resources.

Decreasing the size (in space and time) of the super-ob box from the default size (Fig. 3.6b) to the experimental values in Table 3.1 (2 degrees azimuthal range, 2.5-km radial range, +/- 7.5 minutes, and a minimum of 10 samples; Fig. 3.6c) reduces the volume for which the observations are averaged and as expected are more representative of the observations (Fig. 3.6a). These settings are likely too fine for a 3-km grid, because several grid points are needed to accurately represent a wave, and therefore still contains

some amount of representativeness error associated with a 3-km model. This decrease of about a factor of two in the smoothing parameters resulted in an increase by a factor of four in the observation density which also increased the computational cost of running the analysis (statistics on the computational efficiency were not done).

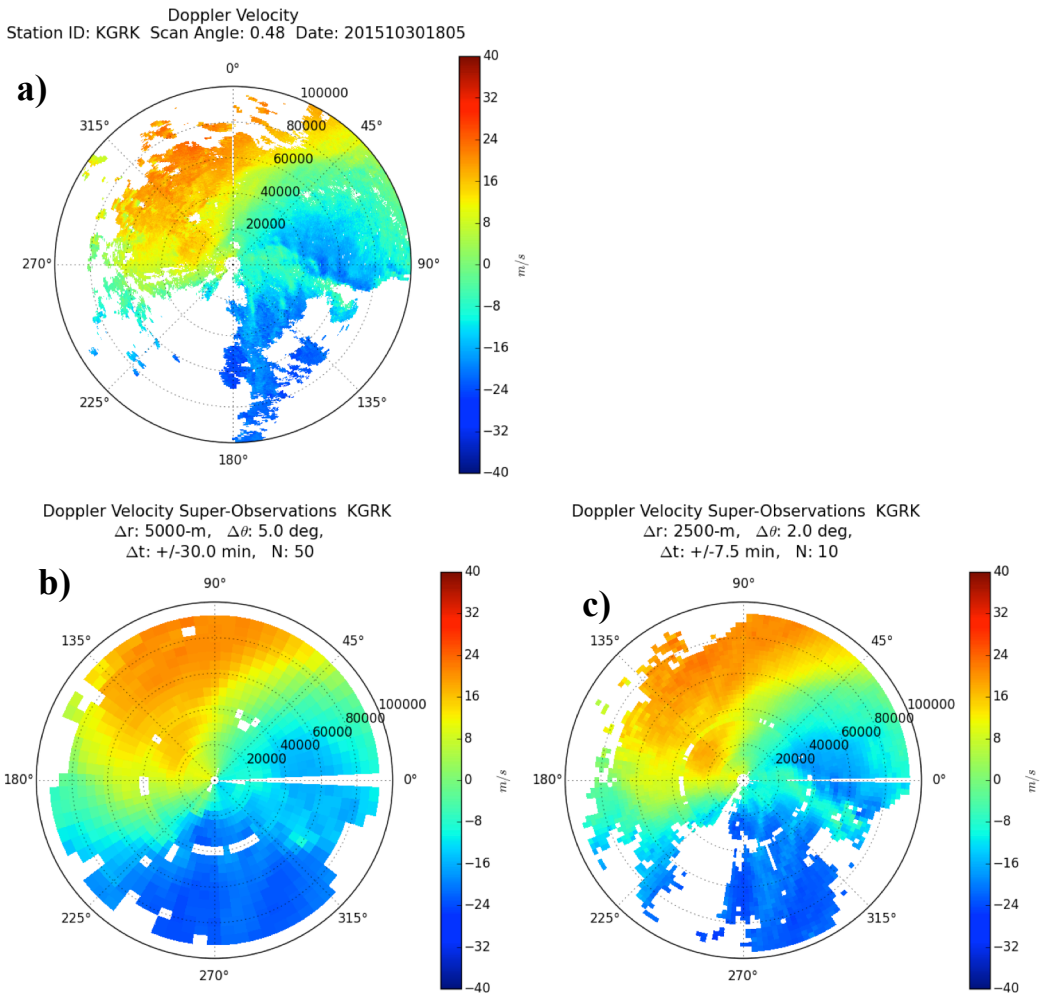

Fig. 3.6 Visualization of the radar observations before and after the GSI super-ob processing. Shown is the Level-II radial wind observation before super-obbing (a) and the default super-ob setting (b) and experimental super-ob settings (c) for the radial winds.

3.4 Analysis Impacts Using Super-Observations from a Single Radar

As discussed in section 2.7, the impacts on the analysis of two other configurations were tested: bypassing the VADqc and reducing the horizontal de-correlation length scale tuning parameters and super-ob parameters. Table 3.2 (bottom section) further summarizes these experiments and their settings.

Table 3.2 Summary of the various parameter settings for each experiment. The top section describes the settings for the single-observation experiments and the bottom section describes the experiments using observations from a single radar and for the retrospective simulations. The default settings/pre-operational configurations for each setting are bolded.

Exp	β_s	VADqc	HZSCL	$\Delta\theta$	Δr	Δt	N
SNGLOB0	**0.25**	No	**0.373, 0.746, 1.500**	**5**	**5000**	**30**	**50**
SNGLOB1	0	No	**0.373, 0.746, 1.500**	**5**	**5000**	**30**	**50**
SNGLOB2	1	No	**0.373, 0.746, 1.500**	**5**	**5000**	**30**	**50**
CTL	**0.25**	**Yes**	**0.373, 0.746, 1.500**	**5**	**5000**	**30**	**50**
HZSCL	**0.25**	No	0.200, 0.500, 0.750	**5**	**5000**	**30**	**50**
SUPOB	**0.25**	No	0.200, 0.500, 0.750	2	2500	7.5	10

3.4.1 Velocity-Azimuth Display Quality Control Impacts on the Analysis

QC is an import aspect when assimilating any type of observation. The radial wind undergoes several QC procedures; however, this study will only focus on one of those procedures. The procedure evaluated in this study uses the VAD winds as a QC mark. This quality control procedure is performed internally in the operational assimilation system (GSI) and was originally developed to detect migrating bird contamination (Collins 2001).

VAD winds are a vertically derived profile of the horizontal wind field based on the radial wind observations and a linearized wind model (Holleman et al. 2005). Linearizing the wind field will inevitably cause deviations from the highly nonlinear radial wind observations. The procedure of the VADqc is to compare the super-obbed radial wind observations to the VAD derived winds. If there are large differences between the super-obs and the VAD winds, then the observations are rejected. In other words, only observations that agree with the VAD winds within some predetermined tolerance are used and might be problematic for convective scale DA. A more specific description of

the VADqc routine is covered by the Development Testbed Center GSI user guide available online at http://www.dtcenter.org/com-GSI/users/docs/.

Removing the VADqc procedure (Fig. 3.7b) resulted in more super-observations getting into the assimilation than when the VADqc procedure is used (Fig. 3.7a). Using the default super-observation values in Table 3.1 (5 degrees azimuthal range, 2.5-km radial range, +/- 30 minutes, and a minimum of 50 samples) there were 9,089 super-observations created and after the VADqc procedure, only 1,490 of those were kept. After additional QC was performed 4 additional super-observations were removed. In the experiments bypassing the VADqc, 7,761 super-observations made it past the remaining QC. As a result, there are differences on the order of ~5 m s^{-1} between VADqc and noVADqc (Fig. 3.7c).

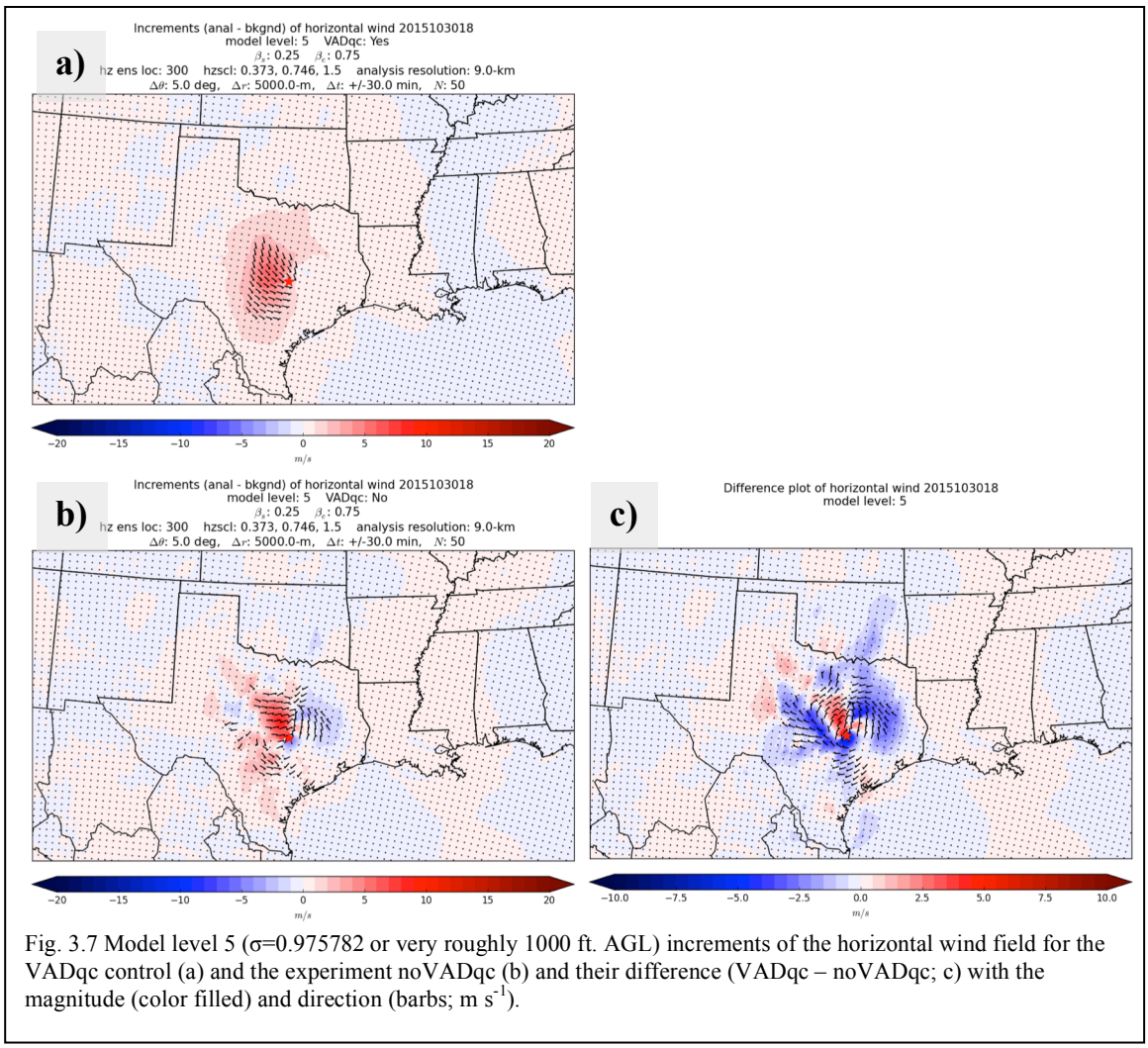

Fig. 3.7 Model level 5 (σ=0.975782 or very roughly 1000 ft. AGL) increments of the horizontal wind field for the VADqc control (a) and the experiment noVADqc (b) and their difference (VADqc – noVADqc; c) with the magnitude (color filled) and direction (barbs; m s^{-1}).

3.4.2 Scaling the Horizontal De-correlation Length Scale Impacts on the Analysis

In DA, a model equivalent is computed for each observation for comparison. The difference between these values is known as the innovation. The innovation is one factor that controls the magnitude of the optimal increment added to the previous guess or forecast. The analysis increment for each observation is not computed for only the initial model grid point used to determine the innovation, but the increment also influences surrounding grid points. The way that the increment is spread depends on many factors such as the specific DA method as well as through correlation relationships through the static and/or ensemble background error covariance ($\mathbf{B_f}$ and $\mathbf{L}$ from Eq. 1 respectively). In DA systems, each analysis control variable has its own estimated de-correlation length scale. This is the e-folding distance at which an analysis increment will have an impact on surrounding grid points.

In this study, tuning parameters for the horizontal de-correlation length scales (configured for the 12-km parent domain) for all variables are adjusted to evaluate their sensitivity on the analysis. These parameters are scalar multipliers used to modify the off-diagonal auto-correlations in the static background error covariance matrix estimated using the NMC method (Parrish and Derber 1992).

There are differences of about 2 m s^{-1} in some areas (Fig. 3.8b) between the default horizontal de-correlation tuning parameter values (0.373, 0.746, and 1.5; Table 3.2; noVADqc; Fig. 3.7b) and the experimental values (0.200, 0.500, 0.750; Table 3.2;

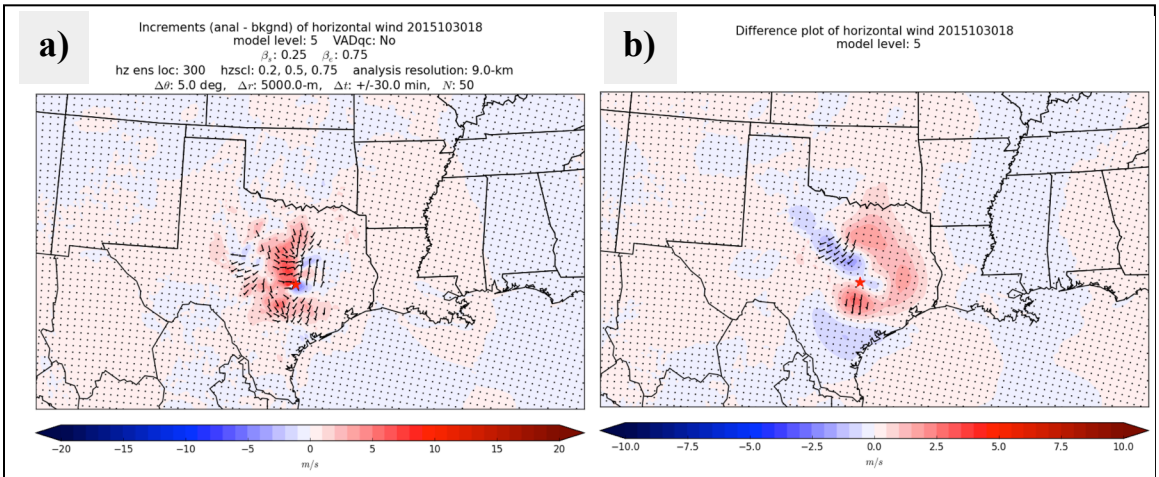

Fig. 3.8 Model level 5 (σ=0.975782 or very roughly 1000 ft. AGL) analysis increments for HZSCL (a) and the difference (b) from noVADqc (as in Fig. 3.7b; Table 3.2). The magnitude of increment/difference (color filled) and direction (barbs; m s^{-1})

HZSCL; Fig. 3.8a) despite that the background error covariance is weighted 75% toward the ensemble error covariance and 25% toward the static.

It is difficult to know if this resulted in a better analysis because the true state is unknown. But this motivates many questions such as what length scale should be used, should we also tuned the vertical length scale, should different analysis control variables be used (different control variables may have different de-correlation length scales), and what localization should be used for our ensemble (this is the ensemble counterpart to the static error de-correlation length)?

3.4.3 Super-Observation Density Impacts on the Analysis

Up until now, only the radial wind QC adjustments and the sensitivity to the horizontal de-correlation length scales have been briefly explored in a single experimental analysis. In this section the impact of changing the super-observation density, similarly to what was done in section 3.3, will be tested. The settings for this experiment are described in Table 3.2 (SUPOB). These experimental values were chosen because they were the smallest values that could be used at the time without using an unreasonable amount of computational resources.

It was shown in section 3.3 (Fig. 3.6a-c) that by increasing the super-observation density, more of the storm-scale features could be retained because the averaging is done over a smaller area. Reducing the super-ob box size has multiple trade-offs. With a smaller area to average, there will naturally be fewer observations to average and thus

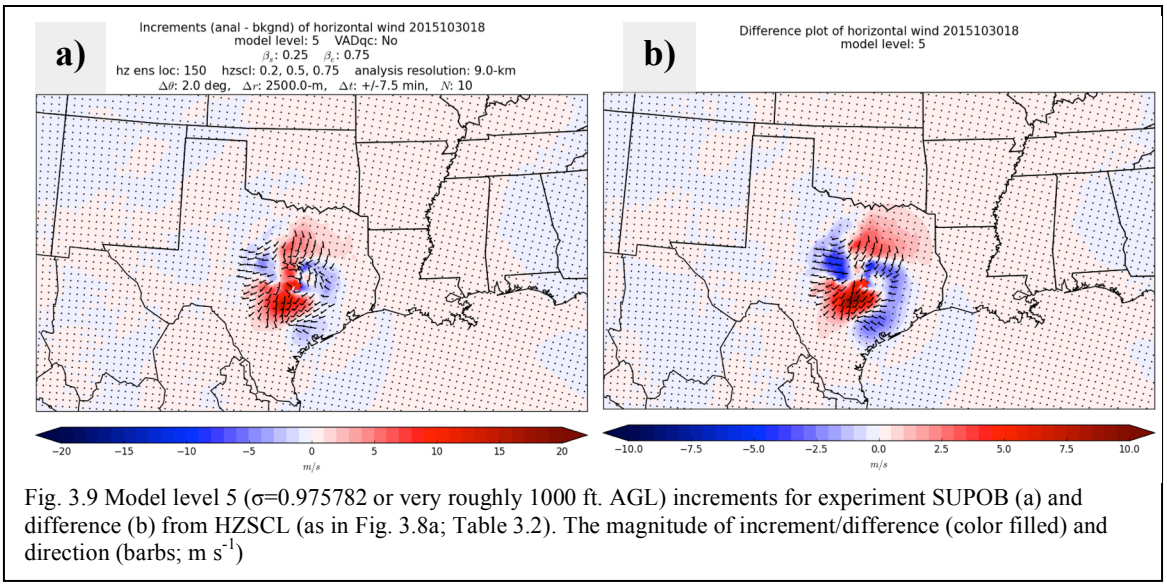

Fig. 3.9 Model level 5 (σ=0.975782 or very roughly 1000 ft. AGL) increments for experiment SUPOB (a) and difference (b) from HZSCL (as in Fig. 3.8a; Table 3.2). The magnitude of increment/difference (color filled) and direction (barbs; m s^{-1})

would be more representative of the observed state. Simultaneously, the super-observations are becoming less representative of what the model can resolve (i.e., representativeness error). Furthermore, the error assigned to the super-ob by Eq. 5 will be more affected by outliers within the grid box and less de-correlation of observation errors.

In this experiment (SUPOB; Fig. 3.9a), there is a large difference of about 5-10 m s^{-1} (Fig. 3.9b) between the SUPOB and HZSCL (Fig. 3.8a) experiments as a result of the increased density of super-observations.

3.5 Forecast Impacts

Retrospective weather forecasts were generated using the NAMRR forecast system simulating the convectively active period 30-31 October 2015 in the southern plains in order to evaluate the impacts of the modifications to the radial wind assimilation. Three experimental configurations were run (Table 3.2 bottom section) and are compared using subjective analyses. These analyses include visual comparisons of 3-hr total accumulated precipitation and 3- and 4-hr simulated radar reflectivity mosaics across each experiment and against observations.

3.5.1 Heavy Precipitation in the Vicinity of Austin and San Antonio, Texas

As described in the case study overview, a storm system organized and intensified at the boundary of the LLJ and the warm front in the vicinity of Austin and San Antonio, Texas painting a bulls-eye of 5+ inches of precipitation over the course of a 3-hr period in that region as shown by observations (Fig. 3.10a). Each of the models has a decent 3-hr forecast for these total amounts and it is hard to discern improvements subjectively. It appears that for both experiments (Fig. 3.10c,d), the bulls-eye is slightly farther north aligning closer to observations than in CTL (Fig. 3.10b).

The 3-hr simulated reflectivity mosaics (Fig. 3.11b-d) also show good agreement with observations over this same period (Fig. 3.11a), in the vicinity of the heavy precipitation. It is important to note that these forecast were initialized during the 1200 UTC NAMRR catch-up cycle, which could play a role in the quality of the forecasts.

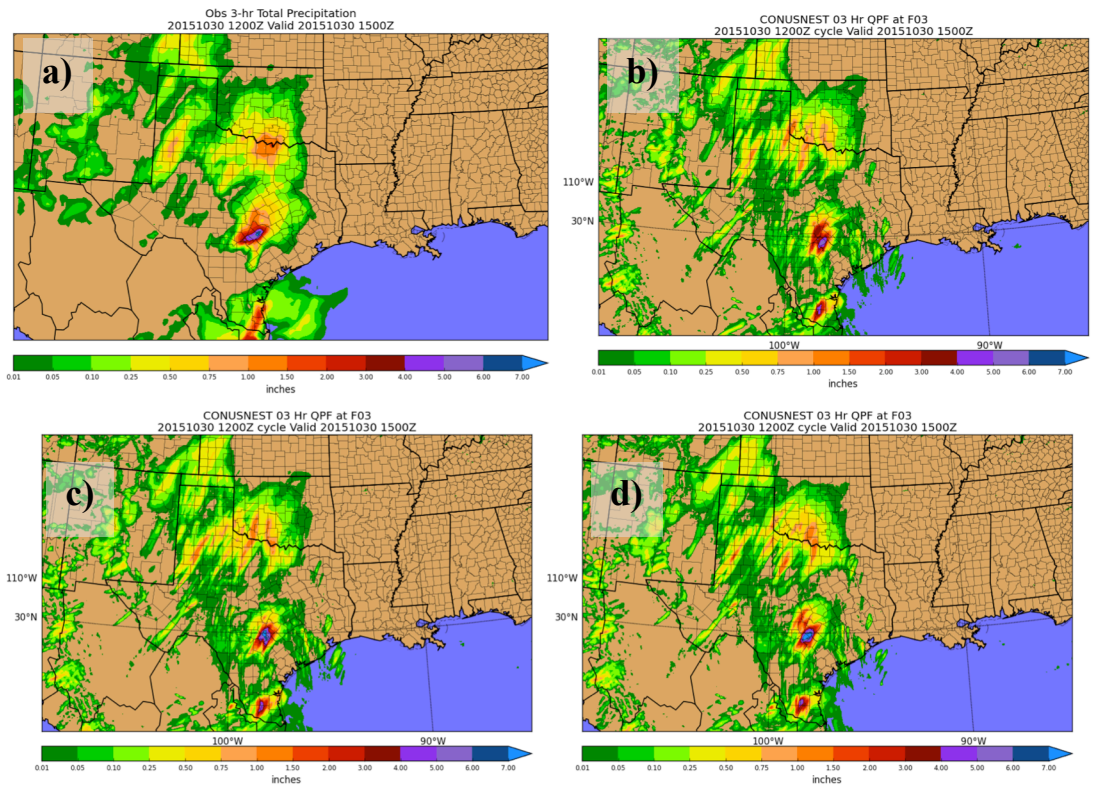

Fig. 3.10 Total 3-hour precipiation (inches) valid 20151030 1500Z. Observations (a; Hou et al. 2014), CTL experiment (b), HZSCL experiment (c), and SUPOB experiment (d). Details about each experiment are given in Table 3.2 bottom section.

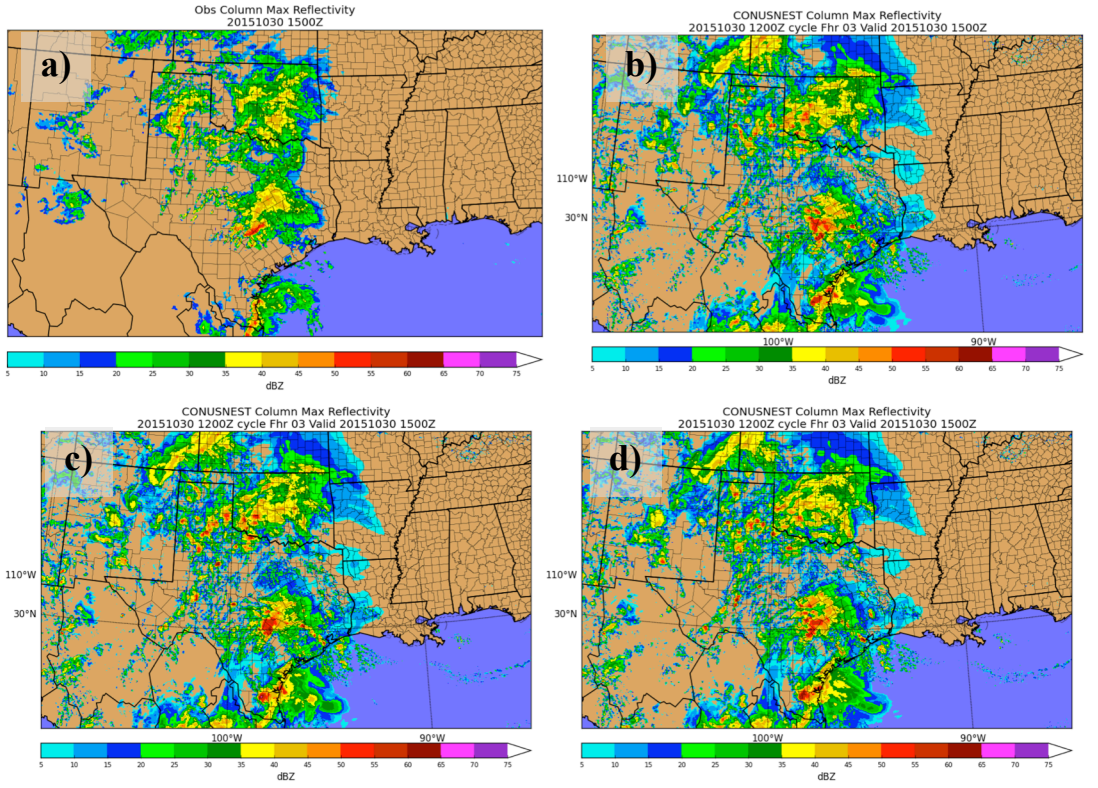

Fig. 3.11 Reflectivity mosaics valid 20151030 1500Z. Observations are shown (a), CTL experiment (b), HZSCL experiment (c), and SUPOB experiment (d). Details about each experiment are given in Table 3.2 bottom section.

The 4-hr simulated reflectivity mosaics from the 1100 UTC cycle (valid at the same time as the previous comparison; Fig. 3.12b-d) that it might be the case that the 1200 UTC catch-up cycle, in addition to more up-to-date observations, allowed the CTL to have less noticeable difference from the experiments. It appears that SUPOB and HZSCL are able to better forecast the heavy precipitation, before the 1200 UTC cycle was available, near Austin and San Antonio, Texas. This is an important result, as the purpose of the hourly-cycles is to benefit from more frequent observations and updates to the forecast between each catch-up cycle. Furthermore, some of the high reflectivity values situated over north central Texas and Oklahoma seem to be slightly more suppressed in the experimental simulations. Although these results are based on only one case study, it is motivating that even with the basic changes made in this study, it might be expected that more sophisticated advancements may have the potential to see even better results.

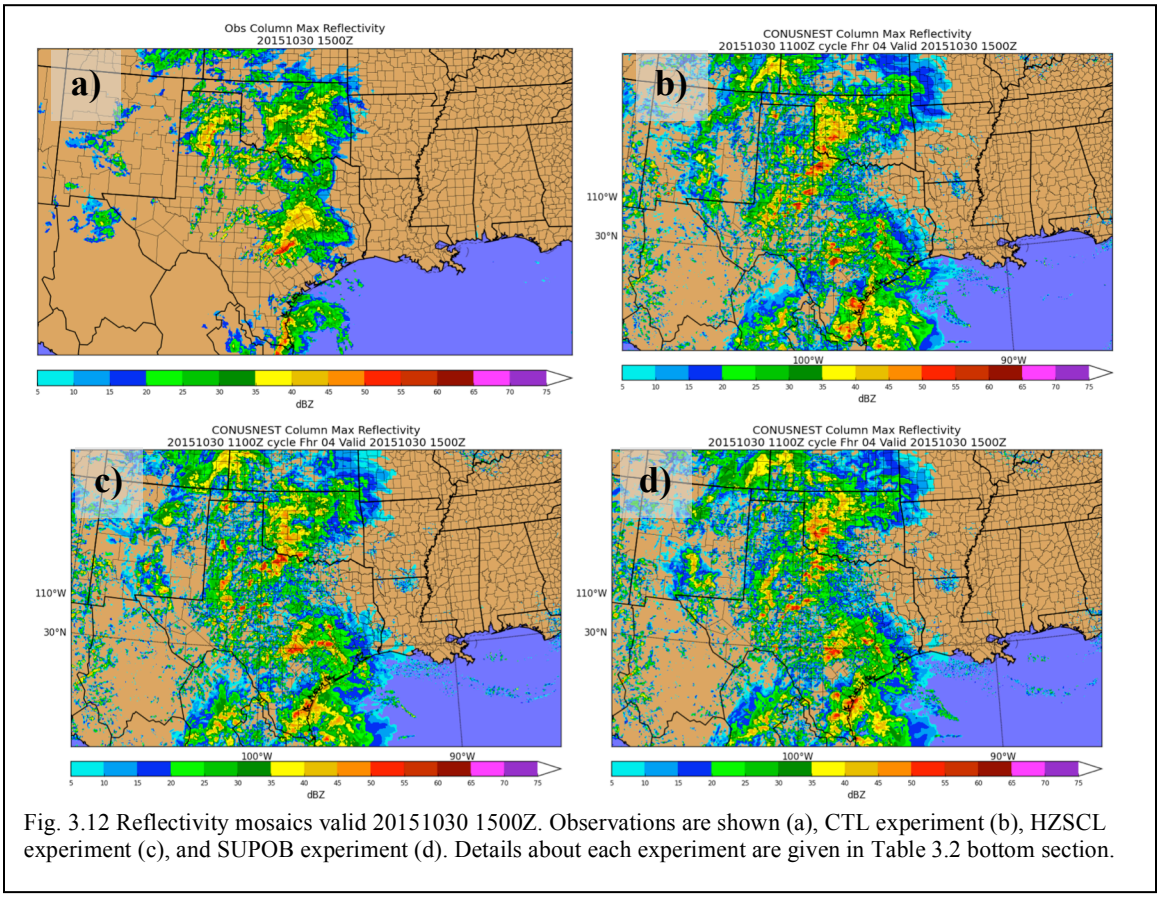

Fig. 3.12 Reflectivity mosaics valid 20151030 1500Z. Observations are shown (a), CTL experiment (b), HZSCL experiment (c), and SUPOB experiment (d). Details about each experiment are given in Table 3.2 bottom section.

3.5.2 Heavy Precipitation in the Vicinity of Houston, Texas

Later during this event, a storm system developed off the Coast of Corpus Cristi, Texas from the effects of a convergent zone entering a very unstable environment. These storms move north-northeastward into the Houston area around 0600 UTC through 0900 UTC. There was intense rainfall (7+ inches) associated with these storms (Fig. 3.3).

The 3-hr forecasted and observed precipitation valid at 0900 UTC are now compared (Fig. 3.13). Each of the simulations appear to be slightly dry compared to the observations near Houston and have spurious rain bands all throughout Texas. It seems that each of these experiments do not pick up on the confluent zone that is apparent in the reflectivity observations (not shown). This zone is the primary forcing mechanism for initiating the storms off the Coast of Corpus Cristi which eventually moved into this region.

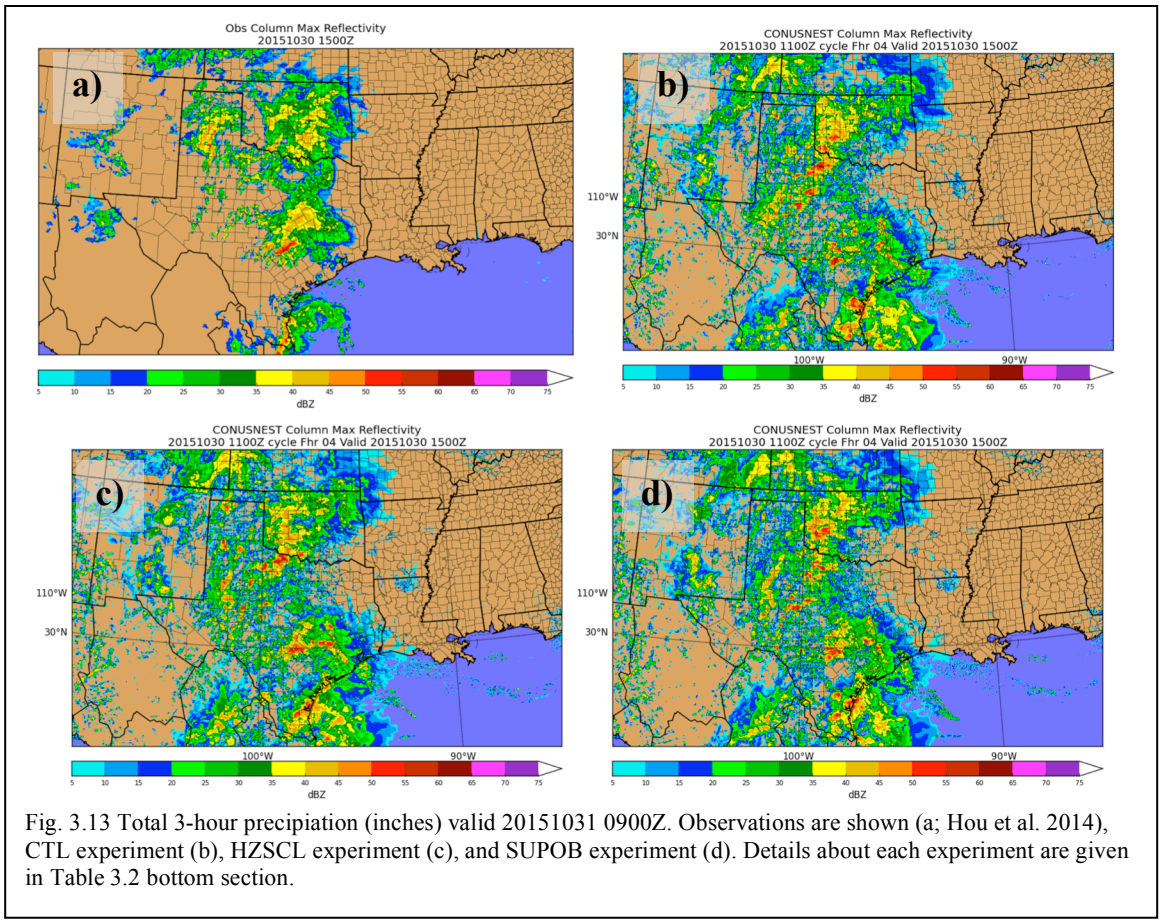

Fig. 3.13 Total 3-hour precipiation (inches) valid 20151031 0900Z. Observations are shown (a; Hou et al. 2014), CTL experiment (b), HZSCL experiment (c), and SUPOB experiment (d). Details about each experiment are given in Table 3.2 bottom section.

Chapter 4. Summary and Conclusions

In this study, the impacts of a reduced horizontal de-correlation length scale for all analysis variables, increased radial wind super-ob density, and no VADqc procedure are examined in a pre-operational configuration of the NAMRR over a 48-hour period using a hybrid 3DEnVar configuration of the GSI. The experiments are verified using subjective analyses; however, objective statistical analyses are expected to be available in the system in the future to further process these results and the results of any future work.

The super-ob technique is graphically interpreted and compared to the raw Level-II radial wind observations. The default settings are shown as well as the settings used for the experiments. The azimuthal and radial super-ob ranges were reduced by a factor of two and the time range by a factor of four. Reducing the spatial coarseness of the observations show, as one would expect, more detail in the observations, but are less representative of what the model can accurately simulate. Determining an optimal setting will require further testing.

The three configurations are tested first using observations from a single radar. The same configurations are then run using the full NAMRR and hybrid 3DEnVar. Reducing each of the parameters and bypassing the VADqc alone did not significantly improve the analysis and forecast results. This is somewhat expected because elevation angles from the radial wind observations > 5-degrees are still ignored as well as many other factors that have yet to be considered (see future work section).

Chapter 5. Future Work

5.1 Assimilation of the Vertical Component of the Radial Wind Observations

This preliminary work barely scratches the surface of improving the radial wind assimilation in the operational GSI for storm-scale NWP. One difficulty, in particular, is that *only the horizontal components of the radial wind observations are assimilated in the GSI*. Furthermore, radar observations from elevation angles greater than 5-degrees are ignored in order to remove effects of vertical motion on the radial wind retrieval because vertical velocity is not a component of the radial wind observation operator or an analysis control variable. The observation operator for radial velocity (V_r) in the GSI is currently given by

$$V_r = u \cos(\theta) \cos(\alpha) + v \sin(\theta) \cos(\alpha) \qquad (6)$$

where u and v are the horizontal wind components, θ is 90-degrees minus the azimuth angle, and α is the elevation angle. By assimilating only the lowest five elevation angles, there is potentially a considerable amount of useful information being discarded (scan angles may exceed 14-degrees). Moreover, ignoring vertical velocity in the vicinity of strongly non-hydrostatic flows, i.e., where vertical velocity can be significant (5-50ms^{-1}), is potentially problematic.

Xiao et al. (2005) assimilated radial wind observations to initialize a 10-km model using scan angles as high as 9-degrees. In their experiments they included vertical velocity with effects of terminal velocity in their observation operator and as an analysis control variable following Sun and Crook (1997). The observation operator was computed as

$$V_r = u \cos(\theta) \cos(\alpha) + v \sin(\theta) \cos(\alpha) + (w - v_T) \sin(\alpha) \qquad (7)$$

which follows as an extension from (Eq. 6) to include the vertical velocity and the effects of terminal velocity v_T by hydrometeors. The terminal velocity is estimated by Sun and Crook (1997) using an analytical equation using a ratio of a base pressure p_0 and the pressure at the surface and the rainwater mixing ratio q_r in units of g kg^{-1}.

$$v_T = 5.40 \left(\frac{p_0}{p}\right)^{0.4} q_r^{0.125} \tag{8}$$

The rainwater mixing ratio q_r can be estimated by a relationship between the reflectivity factor Z from Doppler radar observations using the Marshall-Palmer distribution of raindrop size which is explained more thoroughly by Sun and Crook (1997). If Z is in units of dBZ, then the Z-q_r relationship becomes

$$Z = 43.1 + 17.5 \log(\rho q_r) \tag{9}$$

Certainly, this addition to the radial wind observation operator more accurately describes the observations resulting in less representativeness errors and will not require ad hoc methods to restrict the observation to the lowest 5 degrees in order to limit the vertical component of the observations. A poorly designed observation operator may also result in larger de-correlation length scales (Waller et al. 2015b). Even the lowest scan angles contain at least some vertical component, especially at a sufficient distance from the radar. Thus, with this extension, the horizontal components of the observations will be more appropriate because the vertical component will be taken into account. Although better characterizing the horizontal component is an important outcome, the primary objective of extending the observation operator to three dimensions is to obtain information about vertical velocity. Under the current formulation of the operational GSI analysis system, observations of vertical velocity have no direct connection to the analysis.

Adding vertical velocity as an analysis control variable will allow for the vertical component of the radial wind at higher scan angles to bring information about the vertical velocity into the analysis. It will also help constrain the divergent part of the wind increment through balances prescribed within the ensemble. Furthermore, if a dynamic relationship for vertical velocity and other variables can be applied, it might be possible to begin resolving non-hydrostatic features in the GSI analysis.

According to Janjić and Gall (2012), vertical velocity and its tendency are not considered independent prognostic variables in the NMMB. The hydrostatic and non-hydrostatic pressures and temperature using the hypsometric equation uniquely define the geometric height. Because these three variables are prognostic they can be used to

calculated vertical velocity given the definition of vertical velocity from a reduction of the non-hydrostatic continuity equation

$$w=\frac{1}{g}\left[\left(\frac{\partial\Phi}{\partial t}\right)_s+\mathbf{v}\cdot\nabla_s\Phi+\left(\dot{s}\frac{\partial\pi}{\partial s}\right)\frac{\partial\Phi}{\partial\pi}\right]+W(\lambda,\phi,t) \tag{10}$$

Here, w is the vertical velocity, $\dot{s}$ is the vertical velocity on model surfaces, s is the hydrostatic coordinate system, g is gravity, Φ is geopotential height, **v** is the horizontal wind vector, π is the hydrostatic pressure, λ and ϕ are latitude and longitude, and W is the integration constant that is dependent on the location and time. The vertical velocity must satisfy the prognostic vertical equation of motion. It is expected that replacing the diagnostic vertical velocity and its tendency in the model by what is obtained in the analysis will allow that information to be communicated into the later forecast (Janjić, personal communication). This should, in practice, reduce the amount of spin-up/down early in the forecast so long as a balanced increment can be passed along. Assuming that a relationship between vertical velocity and other variables are introduced, increments of vertical velocity, regardless if used by the model, can benefit other variables in the analysis and retained later in the forecast.

In order to ensure that the aforementioned modifications to the assimilation of the radial wind observations remain dynamically consistent with both reality and the numerical model, dynamical constraints using equations such as the mass continuity and diagnostic pressure equations (Gao et al. 2004 and Ge et al. 2012) and others can be used. Constraints such as these may be incorporated within the variational cost function as a weak constraint.

5.2 Tuning Static Background Error Statistics, De-correlation Length Scales, and Control Variables for Convective Scale DA

For the pre-operational NAMRR, the analysis is computed on a grid that is usually three times coarser than the model grid (e.g., a 3-km grid would have an analysis grid of 9-km). For storm-scale data assimilation, this could degrade the analysis. However, the static background error covariance is estimated for the NAMRR's North American parent domain (Fig. 2.1), a 12-km grid, so changing the analysis grid ratio parameter to anything less would not change the analysis. If it were changed now to match the current model

resolution, it would be effectively wasting three times more computational resources. Furthermore, having the GDAS EnKF (T574, ~45-km in the tropics) does not provide any storm-scale information. To overcome these issues, it might be necessary to run an ensemble with the desired resolution to bring storm-scale, flow-dependency into the analysis as well as to recompute the static covariance for the 3-km grid and tune the localization within the storm-scale ensemble.

It might also be necessary to reconsider the relation by which the horizontal components of the radial wind observations are brought into the analysis. The analysis control variables that control this in the operational GSI are the stream function and unbalanced velocity potential. Sun et al. (2016) suggests the use of momentum control variables, i.e. *u* and *v*, for high-resolution data assimilation for improving precipitation forecasts. In this study, they claim that using stream function and velocity potential will have a larger de-correlation length scale and the use of horizontal momentum control variables allow better fits using radial wind data, and it will improve the 0-12 hour precipitation forecasts. However, there is concern about treating analysis increments of a vector quantity as scalars when updating the analysis. Therefore, it may instead be worth pursuing vorticity and divergence as control variables, something not evaluated in Sun et al. (2016).

5.3 Optimizing the use of the Super-Observations

A better understanding of the super-obbing technique and how to optimally utilize this technique for high-resolution forecasting and ensuring that it de-correlates observational errors will be needed. It might be worthwhile to account for correlated errors in the radial wind observations (Waller et al. 2015a, b) and implement a different super-obbing technique as initially proposed by Lorenc (1981). Instead of averaging the values of the actual observations, this method averages the innovations. This method still accounts for representativeness errors but allows meteorological info to be retained within the super-ob especially if the observation operator is nonlinear. A spectral analysis using various super-ob settings could be done to identify the smallest scale wave that can be represented by the super-obs and will provide the optimal settings for a given model grid resolution. Creating a single observation experiment changing the super-observation

settings may be able to provide an understanding of how this technique accounts for representativeness errors.

5.4 Assimilation Methods and Frequency for Convective Scale DA

In this study, a hybrid 3DEnVar hourly cycling data assimilation method is used and is already a computationally heavy configuration. To make the best use of the radial wind observations, employing a hybrid 4DEnVar data assimilation method with sub-hourly assimilation cycles will likely produce the most robust results (Youssouf and Stensrud 2010; Johnson et al. 2015; Wheatley et al. 2015). In the 3D systems, observations over an assimilation window are all assumed to be valid at the analysis time and may be weighted according to their respective distance from the analysis time. In 4D systems, the observations are used at their appropriate times to fit an analysis trajectory in time; however, in a 4DEnVar system the use of a tangent linear model and its transpose (the adjoint) are not needed. These modifications will require a significant amount of additional computational resources especially due to the introduction of a storm-scale ensemble.

Because of the important role radial wind observations play for initializing storm-scale NWP forecasts, we are motivated to examine several aspects of the radial wind analysis procedure used by the GSI, the data assimilation system used by all atmospheric NWP systems at the National Weather Service. By including the vertical component of the radial wind observations; replacing the stream function and unbalanced velocity potential analysis control variables with vorticity and divergence; introducing vertical velocity as an analysis control variable; utilizing equations to constrain the analysis to be more dynamically consistent with reality and with respect to the model; recomputing the background statistics and generating a convective-scale ensemble for the flow-dependent background statistics; creating super-obs by averaging their innovations; and increasing the temporal frequency of DA cylcing of these observations, it is expected that a more accurate estimate of the true state of the storm-scale environments can be obtained. Thus, if the model is initialized with such a state that it can retain, it is expected that this will lead to improved short-term forecasts of hazardous convective storms relative to what is currently done with the U.S. operational NWP forecast systems.

References

Aksoy, A., D. C. Dowell, and C. Snyder, 2009: A multicase comparative assessment of the ensemble Kalman filter for assimilation of radar observations. Part I: Storm-scale analyses. *Mon. Wea. Rev.*, **137**, 1805–1824, doi:10.1175/2008MWR2691.1.

Aksoy, A., D. C. Dowell, and C. Snyder, 2010: A multicase comparative assessment of the ensemble Kalman filter for assimilation of radar observations. Part II: Short-range ensemble forecasts. *Mon. Wea. Rev.*, **138**, 1273–1292, doi:10.1175/2009MWR3086.1.

Aligo, E., B. Ferrier, J. Carley, E. Rogers, M. Pyle, S. J. Weiss, and I. L. Jirak, 2014: Modified Microphysics for use in high-resolution NAM forecasts. *27th Conference on Severe Local Storms*, Madison, WI, Amer. Meteor. Soc. [Available online at https://ams.confex.com/ams/27SLS/webprogram/Paper255732.html.]

Alpert, J. C. and V. K. Kumar, 2007: Radial Wind Super-Obs from the WSR-88D Radars in the NCEP Operational Assimilation System.*Mon. Wea. Rev.*, **135**, 1090–1109. doi: http://dx.doi.org/10.1175/MWR3324.1

Buehner, M., P. L. Houtekamer, C. Charette, H. L. Mitchell, and B. He, 2010: Intercomparison of variational data assimilation and the ensemble Kalman filter for global deterministic NWP. Part II: One-month experiments with real observations. *Mon. Wea. Rev.*, **138**, 1567–1586, doi:10.1175/2009MWR3158.1.

Carley, J. R., 2012: Hybrid ensemble-3DVar radar data assimilation for the short-term prediction of convective storms. Ph.D. dissertation, Department of Earth, Atmospheric, and Planetary Sciences, Purdue University, 205 pp.

Carley, J. R., E. Rogers, B. S. Ferrier, E. Aligo, W. S. Wu, S. Liu, M. Pyle, X. Zhang, and G. DiMego, 2015: Ongoing development of the hourly-updated version of the NAM forecast system. *27th Conf. on Weather Analysis and Forecasting/23rd Conf. on Numerical Weather Prediction*, Chicago, IL, Amer. Meteor. Soc. **2A.1**.

Caya, A., J. Sun, and C. Snyder, 2005: A comparison between the 4DVAR and the ensemble Kalman filter techniques for radar data assimilation. *Mon. Wea. Rev.*, **133**, 3081–3094, doi:10.1175/MWR3021.1.

Collins, W. G., 2001: The quality control of velocity azimuth display (VAD) winds at the National Centers for Environemtal Prediction. Preprints, *11th Symp. on Meteorological Observations and Instrumentation,* Albuquerque, NM, Amer. Meteor. Soc., CD-ROM, 9.2.

Djalalova, I. V., J. Olson, J. R. Carley, L. Bianco, J. M. Wilczak, Y. Pichugina, R. Banta, M. Marquis, and J. Cline, 2016: The POWER experiment: Impact of assimilation of network of coastal wind profiling radars on simulating offshore winds in and

above the wind turbine layer. *Wea. Forecasting.* doi: http://dx.doi.org/10.1175/WAF-D-15-0104.1

Dowell, D. C., L. J. Wicker, and D. J. Stensrud, 2004: High resolution analyses of the 8 May 2003 Oklahoma City storm. Part II: EnKF data assimilation and forecast experiments. Preprints, 22nd Conf. on Severe Local Storms, Hyannis, MA, Amer. Meteor. Soc., 12.5. [Available online at http://ams.confex.com/ams/pdfpapers/81393.pdf].

Dowell, D. C., and L. J. Wicker, 2009: Additive noise for storm-scale ensemble data assimilation. *J. Atmos. Oceanic Technol.*, **26**, 911–927, doi:10.1175/2008JTECHA1156.1.

Droegmeier KK. 1997. The munerical prediction of thunderstorms: Challenges, potential benefit, and results from real-time operational test. *WMO Bull.* **46**: 324–336.

Ek, M. B., K. E. Mitchell, Y. Lin, E. Rogers, P. Grunmann, V. Koren, G. Gayno, and J. D. Tarpley, 2003: Implementation of Noah land surface model advances in the National Centers for Environmental Prediction operational mesoscale Eta model. *J. Geophys. Res.*, 108 (D22), 16, doi:10.1029/2002JD003296.

Gao, J., M. Xue, K. Brewster, and K. K. Droegemeier, 2004: A Three-Dimensional Variational Data Analysis Method with Recursive Filter for Doppler Radars. *J. Atmos. Oceanic Technol.*, **21**, 457–469. doi: http://dx.doi.org/10.1175/1520-0426(2004)021<0457:ATVDAM>2.0.CO;2

Gao, J., and M. Xue, 2008: An efficient dual-resolution approach for ensemble data assimilation and tests with simulated Doppler radar data. *Mon. Wea. Rev.*, **136,** 945–963.

Gao, J. and D. J. Stensrud, 2014: Some Observing System Simulation Experiments with a Hybrid 3DEnVAR System for Storm-Scale Radar Data Assimilation. *Mon. Wea. Rev.*, **142**, 3326–3346. doi: http://dx.doi.org/10.1175/MWR-D-14-00025.1

Ge, G., J. Gao, and M. Xue, 2012: Diagnostic Pressure Equation as a Weak Constraint in a Storm-Scale Three-Dimensional Variational Radar Data Assimilation System. *J. Atmos. Oceanic Technol.*, **29**, 1075–1092 doi: http://dx.doi.org/10.1175/JTECH-D-11-00201.1

Hou, D., and Coauthors, 2014: Climatolog-calibrated precipitation analysis at fine scales: Statistical adjustment of state IV toward CPC gauge-based analysis. *J. Hydrometeor.*, **15**, 2542-2557, doi: 10.1175/JHM-D-11-0140.1

Holleman, I., H. Benschop, and J. van der Meulen, 2005: Upper Air Wind Measurements by Weather Radar. *In WMO Technical Conference on Meteorological and Environmental Instruments and Methods of Observation*.

Hu, M., M. Xue, and K. Brewster, 2006: 3DVAR and Cloud Analysis with WSR-88D Level-II Data for the Prediction of the Fort Worth, Texas, Tornadic Thunderstorms. Part I: Cloud Analysis and Its Impact. *Mon. Wea. Rev.*, **134**, 675–698. doi: http://dx.doi.org/10.1175/MWR3092.1

Iacono, M. J., J. S. Delamere, E. J. Mlawer, M. W. Shephard, S. A. Clough, and W. D. Collins, 2008: Radiative forcing by long-lived greenhouse gases: Calculations with the AER radiative transfer models, *J. Geophys. Res.*, **113**.

Ide, K., P. Courtier, M. Ghil, and A. Lorenc, 1997: Unified notation for data assimilation: Operational, sequential and variational. J. Meteor. Soc. Japan, 75, 181–189.

Janjić, Z. I., 1994: The Step–Mountain Eta Coordinate Model: Further developments of the convection, viscous sublayer, and turbulence closure schemes. *Mon. Wea. Rev.*, **122**, 927– 945.

Janjić, Z. I., 2001: Nonsingular implementation of the Mellor-Yamada level 2.5 scheme in the NCEP meso model. NCEP Office Note, 91 pp. [437].

Janjić, T., and S. E. Cohn, 2006: Treatment of observation error due to unresolved scales in atmospheric data assimilation.*Mon. Wea. Rev.*, **134**, 2900–2915.

Janjić Z. and R. Gall, 2012: Scientific Documentation of the NCEP Nonhydrostatic Multiscale Model on the B grid (NMMB). Part 1 Dynamics. *NCAR Technical Note.* [Available online at http://www.dtcenter.org/nems-nmmb/users/docs/overview.php]

Johnson, A., X. Wang, J. R. Carley, L. J. Wicker, and C. Karstens, 2015: A comparison of multiscale GSI-based EnKF and 3DVar data assimilation using radar and conventional observations for midlatitude convective-scale precipitation forecasts. *Mon. Wea. Rev.*, **143**, 3087–3108, doi:10.1175/MWR-D-14-00345.1.

Jung, Y., G. Zhang, and M. Xue, 2008: Assimilation of simulated polarimetric radar data for a convective storm using the ensemble Kalman filter. Part I: Observation operators for reflectivity and polarimetric variables. *Mon. Wea. Rev.*, **136**, 2228–2245, doi:10.1175/2007MWR2083.1.

Kleist, D. T., D. F. Parrish, J. C. Derber, R. Treadon, W.-S. Wu, and S. Lord, 2009: Introduction of the GSI into the NCEP Global Data Assimilation System. *Wea. Forecasting*, **24**, 1691–1705. doi: http://dx.doi.org/10.1175/2009WAF2222201.1

Kleist, D. T. and K. Ide, 2015a: An OSSE-Based Evaluation of Hybrid Variational–Ensemble Data Assimilation for the NCEP GFS. Part I: System Description and 3D-Hybrid Results. *Mon. Wea. Rev.*, **143**, 433–451. doi: http://dx.doi.org/10.1175/MWR-D-13-00351.1

Kleist, D. T. and K. Ide, 2015b: An OSSE-Based Evaluation of Hybrid Variational–Ensemble Data Assimilation for the NCEP GFS. Part II: 4DEnVar and Hybrid Variants. *Mon. Wea. Rev.*, **143**, 452–470. doi: http://dx.doi.org/10.1175/MWR-D-13-00350.1

Li, Y., X. Wang, and M. Xue, 2012: Assimilation of radar radial velocity data with the WRF hybrid ensemble–3DVAR system for the prediction of Hurricane Ike (2008). *Mon. Wea. Rev.*, **140**, 3507–3524.

Liu, S., M. Xue, J. Gao, and D. Parrish, 2005: Analysis and impact of super-obbed Doppler radial velocity in the NCEP Grid-point Statistical Interpolation (GSI) analysis system. Preprints, *21st Conf. on Weather Analysis and Forecasting/17th Conf. on Numerical Weather Prediction,* Washington, DC, Amer. Meteor. Soc., 13A.4. [Available online at https://ams.confex.com/ams/WAFNWP34BC/techprogram/paper_94230.htm.]

Liu, C., Q. Xiao, and B. Wang, 2008: An ensemble-based four-dimensional variational data assimilation scheme. Part I: Technical formulation and preliminary test. *Mon. Wea. Rev.*, **136,** 3363–3373.

Liu, C., Q. Xiao, and B. Wang, 2009: An ensemble-based four-dimensional variational data assimilation scheme. Part II: Observing system simulation experiments with Advanced Research WRF (ARW). *Mon. Wea. Rev.*, **137,** 1687–1704.

Liu, C., and Q. Xiao, 2013: An ensemble-based four-dimensional variational data assimilation scheme. Part III: Antarctic applications with Advanced Research WRF using real data. *Mon. Wea. Rev.*, **141**, 2721–2739, doi:10.1175/MWR-D-12-00130.1.

Lorenc, A. C., 1981: A global three-dimensional multivariate statistical interpolation scheme. *Mon. Wea. Rev.*, **109,**701–721.

Lorenc, A. C., 2003: The potential of the ensemble Kalman filter for NWP—A comparison with 4D-VAR. *Quart. J. Roy. Meteor. Soc.*, **129**, 3183–3203, doi:10.1256/qj.02.132.

Lorenc, A. C., 2013: Recommended nomenclature for EnVar data assimilation methods. *Research Activities in Atmospheric and Oceanic Modeling,* WGNE, 2 pp. [Available online at http://www.wcrp-climate.org/WGNE/BlueBook/2013/individual-articles/01_Lorenc_Andrew_EnVar_nomenclature.pdf.]

Lu, H., and Q. Xu, 2009: Trade-offs between observation accuracy and resolutions in configuring phased-array radar velocity scans for ensemble-based storm-scale data assimilation. *J. Appl. Meteor. Climatol.*, **48**, 1230–1244, doi:10.1175/2008JAMC2009.1.

Parrish, D. F. and J. C. Derber, 1992: The National Meteorological Center's Spectral Statistical-Interpolation Analysis System. *Mon. Wea. Rev.*,**120**, 1747–1763. doi: http://dx.doi.org/10.1175/1520-0493(1992)120<1747:TNMCSS>2.0.CO;2

Purser, R. J., D. Parrish and M. Masutani, 2000: Meteorological observational data compression; an alternative to conventional "super-obbing". Office Note 430, National Centers for Environmental Prediction, Camp spring, MD [Available online at http://www.lib.ncep.noaa.gov/ncepofficenotes/2000s/].

Rihan, F. A., C. G. Collier, S. P. Ballard, and S. J. Swarbrick, 2008: Assimilation of Doppler radial winds into a 3D-Var system: Errors and impact of radial velocities on the variational analysis and model forecasts. *Quart. J. Roy. Meteor. Soc.*,**134**, 1701–1716.

Rogers, E., and Coauthors, 2009: The NCEP North American Mesoscale modeling system: 645 Recent changes and future plans. Preprints, 23rd Conf. on Weather Analysis and 646 Forecasting/19th Conf. on Numerical Weather Prediction, Omaha, NE, Amer. Meteor. Soc., 647 **2A.4**. [Available online at http://ams.confex.com/ams/pdfpapers/154114.pdf].

Rogers, E., B. Ferrier, Z. Janjić, W. S. Wu, and G. DiMego, 2014: The NCEP North American 650 Mesoscale (NAM) Analysis and Forecast System: Near-term plans and future evolution into a 651 high-resolution ensemble. *26th Conf. on Weather Analysis and Forecasting/22nd Conf. on* 652 *Numerical Weather Prediction,* Atlanta, GA, Amer. Meteor. Soc., **J1.3**.

Schwartz, C. S., and Z. Liu, 2014: Convection-permitting forecasts initialized with continuously cycling limited-area 3DVAR, ensemble Kalman filter, and “hybrid” variational-ensemble data assimilation systems. *Mon. Wea. Rev.*, **142**, 716–738, doi:10.1175/MWR-D-13-00100.1.

Simonin, D., S. P. Ballard, and Z. Li, 2014: Doppler radar radial wind assimilation using an hourly cycling 3D-Var with a 1.5 km resolution version of the Met Office Unified Model for nowcasting. *Quart. J. Roy. Meteor. Soc.*, in press, doi:10.1002/qj.2298.

Snyder, C., and F. Zhang, 2003: Assimilation of simulated Doppler radar observations with an ensemble Kalman filter. *Mon. Wea. Rev.*, **131**, 1663–1677

Stensrud, D. J. and J. Gao, 2010: Importance of Horizontally Inhomogeneous Environmental Initial Conditions to Ensemble Storm-Scale Radar Data Assimilation and Very Short-Range Forecasts. *Mon. Wea. Rev.*, **138**, 1250–1272 doi: http://dx.doi.org/10.1175/2009MWR3027.1

Stensrud, D. J., and Coauthors, 2013: Progress and challenges with Warn-on-Forecast. *Atmos. Res.*, **123**, 2–16.

Sun, J., and N. A. Crook, 1997: Dynamical and microphysical retrieval from Doppler radar observations using a cloud model and its adjoint. Part I: Model development and simulated data experiments. *J. Atmos. Sci*, **54,** 1642–1661.

Sun, J., 2005: Convective-scale assimilation of radar data: progress and challenges. *Quart. J. Roy. Meteorol. Soc.*, **131**: 3439–3463. doi: 10.1256/qj.05.149

Sun, J., W. Tong, Y. Zhang, C.-Y. Lin, D. Xu 2016: Comparison of the Impacts of Momentum Control Variables on High-Resolution Variational Data Assimilation and Precipitation Forecasting. *Mon. Wea. Rev.* **144**: 149-169.

Tong, M., and M. Xue, 2005: Ensemble Kalman filter assimilation of Doppler radar data with a compressible nonhydrostatic model: OSS experiments. *Mon. Wea. Rev.*, **133**, 1789–1807.

Waller, J. A. 2013: Using observations at different spatioal scales in data assimilation for environmental prediction. PhD thesis, University of Reading, Department of Mathematics and Statistics. [Available online at: http://www.reading.ac.uk/maths-and-stats/research/theses/mathsphdtheses.aspx.]

Waller, J.A., S. L. Dance, A. S. Lawless, N. K. Nichols, 2014a: Estimating correlated observation error statistics using and ensmeble transform Kalman filter. *Tellus A* doi: http://dx.doi.org/10.3402/tellusa.v66.23294.

Waller, J.A., S. L. Dance, A. S. Lawless, N. K. Nichols, J. R. Eyre, 2014b: Representativity error for temperature and humidity using the Met Office high-resolution model. *Quart. J. Roy. Meteor. Soc.*, **140**, 1189-1197, doi: 10.1002/qj.2207.

Waller, J. A., S. L. Dance, and N. K. Nichols, 2015a: Theoretical insight into diagnosing observation error correlations using observation-minus-background and observation-minus-analysis statistics. *Quart. J. Roy. Meteor. Soc.,* **142A**, 418-431.

Waller, J. A., D. Simonin, S. L. Dance, N. K. Nichols, S. P. Ballard, 2015b: Diagnosing observation error correlations for Doppler radar radial winds in the Met Office UKV model using observation-minus-background and observation-minus-analysis statistics. *Pre-print, submitted 30 September 2015*. [Available on line: http://centaur.reading.ac.uk/50577/.]

Wang, X., T. M. Hamill, J. S. Whitaker, and C. H. Bishop, 2007: A comparison of hybrid ensemble transform Kalman filter–OI and ensemble square-root filter analysis schemes. *Mon. Wea. Rev.*, **135**, 1055–1076, doi:10.1175/MWR3307.1.

Wang, X., D. Barker, C. Snyder, and T. M. Hamill, 2008a: A hybrid ETKF–3DVAR data assimilation scheme for the WRF model. Part I: Observing system simulation experiment. *Mon. Wea. Rev.*, **136**, 5116–5131, doi:10.1175/2008MWR2444.1.

Wang, X., 2010: Incorporating ensemble covariance in the Gridpoint Statistical Interpolation (GSI) variational minimization: A mathematical framework. *Mon. Wea. Rev.*, **138**, 2990–2995.

Wang, X., D. Parrish, D. T. Kleist, and J. Whitaker, 2013: GSI 3DVar-Based Ensemble–Variational Hybrid Data Assimilation for NCEP Global Forecast System: Single-Resolution Experiments. *Mon. Wea. Rev.*, **141**, 4098–4117. doi: http://dx.doi.org/10.1175/MWR-D-12-00141.1

Wheatley, D. M., K. H. Knopfmeier, T. A. Jones, and G. J. Creager, 2015: Storm-scale data assimilation and ensemble forecasting with the NSSL Experimental Warn-on-Forecast System. Part I: Radar data experiments. *Wea. Forecasting*, **30**,1795–1817, doi:10.1175/WAF-D-15-0043.1.

Wu, W.-S., R. J. Purser, and D. F. Parrish, 2002: Three-Dimensional Variational Analysis with Spatially Inhomogeneous Covariances. *Mon. Wea. Rev.*, **130**, 2905–2916. doi: http://dx.doi.org/10.1175/1520-0493(2002)130<2905:TDVAWS>2.0.CO;2

Xiao, Q., Y.-H. Kuo, J. Sun, W.-C. Lee, E. Lim, Y.-R. Guo, and D. M. Barker, 2005: Assimilation of Doppler Radar Observations with a Regional 3DVAR System: Impact of Doppler Velocities on Forecasts of a Heavy Rainfall Case. *J. Appl. Meteor.*, **44**, 768–788. doi: http://dx.doi.org/10.1175/JAM2248.1

Xue, Q., H. Lu, S. Gao, M. Xue, and M. Tong, 2008: Time-expanded sampling for ensemble Kalman filter: Assimilation experiments with simulated radar observations. *Mon. Wea. Rev.*, **136,** 2651–2667.

Yussouf, N., and D. J. Stensrud, 2010: Impact of phased-array radar observations over a short assimilation period: Observing system simulation experiments using an ensemble Kalman filter. *Mon. Wea. Rev.*, **138**, 517–538, doi:10.1175/2009MWR2925.1.

Zhang, M., and F. Zhang, 2012: E4DVar: Coupling an ensemble Kalman filter with four-dimensional variational data assimilation in a limited-area weather prediction model. *Mon. Wea. Rev.*, **140**, 587–600.

Zhang, F., M. Zhang, and J. Poterjoy, 2013: E3DVar: Coupling an ensemble Kalman filter with three-dimensional variational data assimilation in a limited-area weather prediction model and comparison to E4DVar. *Mon. Wea. Rev.*, **141**, 900–917, doi:10.1175/MWR-D-12-00075.1.